# DNS of Surface Textures to Control the Growth of Turbulent Spots

## by

## James Stephen Strand, B. S.

## Thesis

Presented to the Faculty of the Graduate School of

The University of Texas at Austin

in Partial Fulfillment

of the Requirements

for the Degree of

## Master of Science in Engineering

## The University of Texas at Austin

## December 2007

**DNS of Surface Textures to Control the Growth of Turbulent Spots**

**Approved by
Supervising Committee:**

# Dedication

This thesis is dedicated to my parents, Mark and Connie Strand.

# Acknowledgements

December 2007

# Abstract

## DNS of Surface Textures to Control the Growth of Turbulent Spots

James Stephen Strand, M. S. E.

The University of Texas at Austin, 2007

Supervisor:  David Goldstein

A spectral DNS code was used to study the growth and spreading of turbulent spots in a nominally laminar, zero-pressure gradient boundary layer.  In addition to the flat wall case, the interaction of these spots with riblets, fins, and "spanwise-damping fins" was examined.  The flat plate, surface textures, and initial spot perturbation were simulated via an immersed boundary method, and a "suction-wall" allowed the available channel code to model a boundary layer.  In all cases, self-similar arrowhead shaped spots formed.  The spanwise-damping fins were very effective; the tallest damping fins were able to completely halt spot spreading.  A decrease in spreading angle was also observed for several of the cases with real fins and with riblets.  The best case of the real fins decreased the spreading angle 19% from the flat wall value, and the best case of the riblets decreased the spreading angle by 12%.  A set of simulated fluid particles were tracked as they moved through the time-developing flowfield, and an analysis of their motion led to the conclusion that turbulent spots spread primarily by destabilizing the surrounding boundary layer rather than by turbulent diffusion.

# Table of Contents

# Nomenclature

$U_\infty$ = free-stream velocity
$U$ = streamwise velocity
$V$ = wall-normal (vertical) velocity
$W$ = spanwise velocity
$\delta_o^*$ = boundary layer displacement thickness at the location of the perturbation
$\delta_o$ = boundary layer 99% thickness at the location of the perturbation
$v$ = kinematic viscosity
$\eta$ = similarity variable for the Blasius solution (see Eq. 2)
$h$ = surface texture height
$s$ = surface texture crest-to-crest spacing
t = time
x = streamwise coordinate
y = wall-normal coordinate
z = spanwise coordinate

# Chapter 1:  Introduction

**TURBULENT SPOTS**

When fluid flows over a solid surface, provided that the Reynolds number is large (>> 1), a thin boundary layer forms.  While flow in the freestream is essentially shear-free, flow in the boundary layer is strongly affected by viscous forces.  The flowfield within the boundary layer meets the no-slip condition on the solid surface, and asymptotically approaches the freestream conditions as the distance from the surface increases.

For values of $Re_x$ ( $Re_x = U_\infty x/\nu$, where $U_\infty$ is the freestream velocity, $x$ is the distance from the leading edge of the solid surface, and $\nu$ is the kinematic viscosity) which are relatively low ($1 \ll Re_x < 10^5\text{-}10^6$ for a flat plate), the flowfield in the boundary layer will remain smooth and laminar.  As $Re_x$ increases a flat plate boundary layer becomes increasingly unstable, and transition to turbulence will eventually occur.  Turbulent spots form naturally during the boundary layer transition process.  As Tollmien-Schlichting waves in a boundary layer grow to large amplitudes, secondary instabilities develop and turbulent spots form.  These spots take on an arrowhead shape, pointing downstream.  Emmons (1951) was the first to describe these spots, and for this reason they are sometimes referred to as Emmons spots.  The spots appear at randomly distributed points and their growth and merging lead to complete transition to turbulence.  A spot appears as a fairly well defined region of turbulence surrounded by laminar flow.

Turbulent spots can also be artificially generated with a localized perturbation in a laminar boundary layer.  Artificially generated spots have been investigated with both experiments and by direct numerical simulation (DNS).  Schubauer and Klebanoff (1955) studied both naturally occurring and artificially generated spots in a low-disturbance

wind tunnel. In order to generate spots artificially, they used an electrical spark for the localized perturbation. Wygnanski et al. (1976) studied artificially generated spots in greater detail, also with an electrical spark for the perturbation. They found that if the perturbation was not strong enough, it was possible that no spot would develop. However, if a spot did form it exhibited self-similar growth, independent of the initial perturbation. Wave packets, which they believed to be TS waves, were observed near the upstream lateral edges of the spot. Wygnanski et al. hypothesized that the breakdown of these wave packets led to the formation of eddies near the spanwise edges of the spot, and thus that the waves were at least partially responsible for the growth of the spots. At the leading edge of the spot a distinct overhang region was observed. In this region the flow immediately above the wall remains laminar, but turbulent fluctuations associated with the spot are found farther from the wall.

Amini and Lespinard (1982) introduced a perturbation by injecting fluid through a hole in a flat plate by means of a loudspeaker. The vertical velocity induced directly above the hole by the injection was as high as $1.25U_\infty$. They were primarily interested in studying a pre-turbulent spot, but their method of perturbation did generate the same arrowhead-shaped turbulent spots as other experiments. Using isodeviation contours of mean velocity, they estimated the spreading angle of the turbulent spot to be ~10°, and the apex angle to be ~30°. For an image of a turbulent spot, with spreading angle, apex angle, etc. labeled, see Fig. 1. Note that in Fig. 1, the spreading angle is measured from the location of the initial perturbation. It is also possible to measure the spreading angle from a virtual origin located upstream or downstream of the initial perturbation. The issue of how to define a virtual origin will be discussed in great detail in Sect. 4.
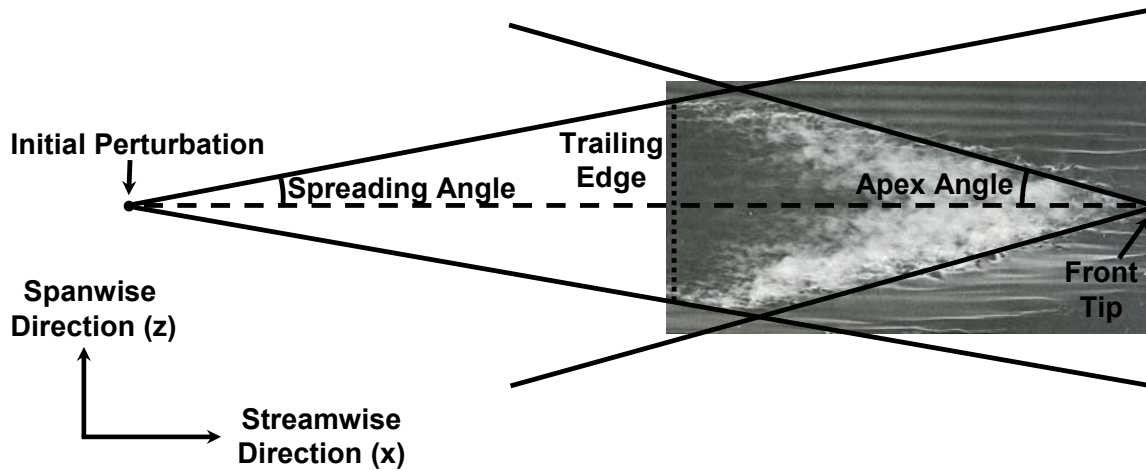
2

Figure 1.1: Schematic top view of a turbulent spot. The spot photograph used here was taken by R. E. Falco using smoke in a wind tunnel flow over a flat plate at $Re_x = 400,000$, and was found in *An Album of Fluid Motion*, by Milton Van Dyke (1982).

DNS has also been used to simulate turbulent spots. Henningson et al. (1987) used a spectral method to simulate the growth and spreading of a turbulent spot in an incompressible flat plate boundary layer. The domain for these simulations was periodic in the streamwise and spanwise directions. To approximate the effect of the thickening of the surrounding boundary layer as the spot moves downstream, a weak body force was applied to the mean flow. The perturbation used to induce the spot was a localized, impulsive body force directed upstream. The force was Gaussian in space, centered at the wall, with a radius of $\delta_o/3$, where $\delta_o$ is the boundary layer thickness at the perturbation location. The spots generated with this perturbation exhibited self-similar growth, as found by experiments. Henningson et al. state that "The turbulent vortical region grows at a half-angle of about 7°. The region in which the velocity is disturbed is wider, about 10°, in good agreement with experimental results." It is not clear how they defined the edge of the *turbulent vortical region*, or how they defined the edge of the *disturbed region*. They found that the growth of the spot became self-similar after $t \approx 100 \; \delta_o/U_\infty$

(the perturbation was initiated at t = 0). Once its growth became self-similar, the spot grew as if from a virtual origin at $t \approx 35 \; \delta_0/U_\infty$ and $x \approx 15 \; \delta_0$ (downstream of the initial perturbation). The trailing edge of the spot moved at $\sim 0.5 U_\infty$, and the leading edge at $\sim 0.83 U_\infty$. Henningson et al. note that these values compare reasonably well with the commonly quoted experimental values of $0.5 U_\infty$ and $0.9 U_\infty$, respectively. They also observed an overhang region at the leading edge of the spot, which is consistent with the experiments of Wygnanski et al.

Singer and Joslin (1994) focused their DNS simulations on the development of a turbulent spot in an incompressible, laminar, zero-pressure-gradient boundary layer. Their domain was periodic in the spanwise direction, and they used a buffer-domain in the streamwise direction to allow for a non-reflective boundary condition on the streamwise velocity. Fluid injection through a short streamwise slot was used to perturb the flow and generate the disturbance that grew into the turbulent spot. They note that some of the structures seen very soon after the fluid injection (especially the "U-shaped vortex", and "necklace vortex") are probably specific to the method of perturbation. Other structures seen later, such as the "quasi-streamwise vortices" appear to be much more generic, and would likely be a part of any young turbulent spot. Many of these quasi-streamwise vortices initially formed under the legs of other streamwise vortices. The interaction of these quasi-streamwise vortices with high pressure regions near the wall frequently led to an ejection of fluid away from the wall, and thus served as a method of vortex regeneration. Viscous entrainment of fluid by nearby vortices also led to the formation of new vortices in some cases, and new vortices were sometimes formed due to the rebound of fluid from the wall. Taken together, the above effects caused the disturbance to spread and grow into a young turbulent spot. Singer and Joslin did not observe a wave packet near the wingtips of the spot, which is consistent with the findings

of the DNS done by Henningson et al.  Singer and Joslin did not report on the apex angle, spreading angle, or leading and trailing edge speeds for the young spot.

Singer (1996) used a more advanced computer, along with the same code and method used by Singer and Joslin, to further simulate the growth of the young turbulent spot.  The simulated spot shared many characteristics with experimentally observed spots (such as those described by Wygnanski et al.), including a distinct overhang region and a calm but non-Blasius region in the wake of the spot.  As in the DNS by Henningson et al., no TS waves were observed at the wingtips of the spot.  Singer notes that the length of his domain in the streamwise direction is only about five times the typical TS wavelength for the simulation Reynolds number.  Furthermore, the calculation is run for less than four times the period of the highest frequency TS wave for the simulation Reynolds number.  Thus, he argues that TS waves have neither enough time nor enough room to grow and propagate.  The spanwise-averaged skin friction coefficient varies widely along the spot centerline, but when this value is averaged over the length of the spot region, the average value is closer to the turbulent value than the laminar one.  A spatially averaged velocity profile does not show a distinct logarithmic region, but Singer states that the flow is likely beginning to develop a log layer.  Singer notes some inconsistencies in the values which have been found by various experiments and simulations for the leading edge and trailing edge speeds and the spreading angle of turbulent spots.  He attributes these inconsistencies primarily to the various methods used to define the edge of the spot.  Some researchers have used isodeviation contours of the streamwise velocity to define the spot edge (this is the method used by Amini and Lespinard), while others (such as Henningson et al.) have used specific isosurfaces of vorticity (or some other pertinent quantity).  Singer defines the leading and trailing edges of the spot as the farthest downstream and upstream locations, respectively, at which the

5

quantity $\left|\dfrac{\partial u}{\partial x}\right|$ along the spot centerline is greater than or equal to an arbitrary threshold value. He notes that this criterion leads to small jump discontinuities in the movement of the leading edge, and larger discontinuities in the movement of the trailing edge. The spanwise edge is defined similarly, except that the edge is defined as the farthest spanwise point (at any x and y location), where the threshold is met. Again, this leads to multiple jump discontinuities, and thus Singer uses linear regression to define the leading edge and trailing edge speeds, and the spreading angle. He calculates a trailing edge speed of $0.63U_\infty$ and a leading edge speed of $0.94U_\infty$. For the spreading angle, he reports values of 3.8° or 6.4°, depending on whether the origin is defined as before or after a particularly large discontinuity in the plot of the spanwise extent of the spot versus the streamwise location of the spanwise edge. Although these values are significantly lower than previously reported experimental values, he argues that this is probably due to the fact that the Reynolds number (based on distance from the perturbation to the measurement location) was about 80,000, which is significantly lower in the simulation than in most experiments (Wygnanski et al.[3] took some data at $Re_x = 120000$, but most of their data was for $Re_x = 600000$).

**DELAYING TRANSITION**

If one could delay or eliminate the onset of transition, the benefits would be appreciable since the viscous drag of a turbulent boundary layer can be four or more times greater than that of a laminar layer. It has been found experimentally, as described by Coustols and Savill (1992) that passive surface textures such as streamwise riblets can reduce the *turbulent* drag on a surface by five to ten percent. Bruce et al. (1993) investigated the drag reduction possible with a wide range of surface textures, including

6

streamwise fins (or blade riblets) and triangular (or sawtooth) riblets. They were able to achieve drag reduction of up to 6% with triangular riblets and 9% with streamwise fins. For a given value of $h^+$ (the height of the textures nondimensionalized by the local mean friction length scale), the drag reduction was strongly dependent on the ratio of texture height to crest-to-crest spacing (h/s). Optimal drag reduction occurred at h/s ≈ 0.7 in the case of triangular riblets and at h/s ≈ 0.5 in the case of streamwise fins. The sharpness of the riblet tip was also important, with sharper riblets providing greater drag reduction for a given h/s. Similarly, thinner fins (thickness/spacing = 0.01) provided greater drag reduction than thicker ones (thickness/spacing = 0.04) for a given h/s.

These experimental results were confirmed numerically by Goldstein et al. (1995). Goldstein and Tuan (1998) also argued that riblets work by damping the near-wall spanwise fluctuations, in agreement with Bruce et al.

If this damping could slow the spanwise spreading of turbulent spots, riblets might be used to significantly delay transition, since in many engineering applications the breakdown to turbulence occurs through the growth and merging of turbulent spots. Furthermore, the riblets would only need to be present in the transition region, so the expense of installing and maintaining riblet film covering this area would be much lower than the expense associated with covering the entire turbulent region.

**THESIS ORGANIZATION**

This thesis is divided into five chapters (with this introduction being Chapter 1). Chapter 2 describes the numerical method used for the simulations and the surface textures which were examined. In Chapter 3 the simulated spots are examined in detail, and are compared to spots observed previously by others in flow visualization. Qualitative comparisons are made between spots over a flat plate and over the surface

textures. Both overall spot characteristics and specific spot structures are discussed, and the interaction of the spots with the textures in the near-wall region is investigated. In Chapter 4, quantitative comparisons are made between spots. The effects of the various textures on spreading angle are studied. Chapter 5 details an effort to track the motion of individual fluid particles as they move in time through the unsteady flowfield created by the developing spot with an eye toward understanding spreading mechanisms. Finally, Chapter 6 discusses the conclusions drawn from the results presented in this work.

# Chapter 2:  Numerical Method

**THE FORCE FIELD MODEL AND SPECTRAL APPROACH**

There exist several approaches to simulating laminar and turbulent boundary layers over textured surfaces.  Goldstein et al. (1993) combined the spectral code described by Handler et al. (1989) (which is based on the spectral method of Kim et al. (1987)) with an immersed boundary technique, to allow for the simulation of laminar or turbulent flows over a multitude of stationary or moving solid surfaces. The approach is particularly flexible and has been successfully tested on a range of turbulent flow configurations over passive surface textures and active MEMS-like devices, as discussed in Goldstein et al. (1995), Goldstein and Tuan (1998), and Colmenero (2004).   The technique for modeling a virtual surface introduces a localized body force field into the Navier Stokes equations.  The force field is made to adapt to the flow and bring it to a specified velocity on the intended points, thereby creating a virtual surface.   This adaptation takes place by means of a two-parameter control scheme, which provides feedback based on both the current velocity at the point, and the prior history of the velocity at that point (an integral term).  The vector equation for the control scheme is

$$\mathbf{F}(\mathbf{x},t) = \alpha \int_0^t \left[\mathbf{U}(\mathbf{x},t') - \mathbf{U_{des}}(\mathbf{x},t')\right]dt' + \beta\left[\mathbf{U}(\mathbf{x},t) - \mathbf{U_{des}}(\mathbf{x},t)\right] \qquad (2.1)$$

where $\mathbf{U}(\mathbf{x},t)$ is the actual velocity vector at the frozen grid point, $\mathbf{U_{des}}(\mathbf{x},t)$ is the desired velocity vector at that point, $\alpha$ and $\beta$ are negative constants, and $\mathbf{F}(\mathbf{x},t)$ is the body force vector applied there.  The gain parameters $\alpha$ and $\beta$ are generally constant in time, but they may be functions of position.   This same base control scheme can be used for other purposes besides creating solid or moving surfaces, as discussed later in this chapter.  For

9

a more detailed explanation of the immersed boundary method employed here, see Goldstein et al. (1993).

## SIMULATION OF A BOUNDARY LAYER

The code described above was originally designed for channel flow, and some modifications were required to allow the simulation of a boundary layer. First, a buffer zone was added (as in Goldstein et al. (2001)) to create the desired inlet Blasius profile. The buffer zone uses the same control scheme as the solid immersed boundaries, but with parameters that are spatially dependent. The velocity gain parameter, $\beta$, at any given location in the buffer zone, is calculated from the equation

$$\beta = 20 \times e^{\left\{-24\left[(x-x_{center})/W\right]^2\right\}} \tag{2.2}$$

where $x_{center}$ is the x location of the midpoint of the buffer zone and W is the buffer zone width. The integral gain parameter, $\alpha$, is zero except in the central third of the buffer zone. In the central third of the zone (where $\left|x - x_{center}\right| \leq W/6$), the equation

$$\alpha = 20 \times e^{\left\{-240\left[(x-x_{center})/W\right]^2\right\}} \tag{2.3}$$

is used, where $x_{center}$ and W are the same as in the equation for $\beta$.

If the velocity were forced to immediately assume the desired profile upon entry to the buffer zone the flow upstream would be altered significantly. This is because even though no forces are applied outside the buffer zone there cannot be a jump discontinuity in incompressible, continuum flow, so the flow upstream must adjust. The use of Gaussians for the gain terms allows the buffer zone to remain relatively "soft". It slowly adjusts the flow as it moves through the zone, so the flow upstream is not significantly affected. At the same time, the integral gain term in the center makes certain that the

10

desired velocity profile is in fact reached inside the buffer zone. See Goldstein et al. (2001) for a more detailed description of the buffer zone.

It was initially assumed that if the boundary layer was thin compared to the channel height, the top wall of the channel would have very little effect. Unfortunately, this is not the case; the boundary layer does not grow downstream as the Blasius solution would predict. Instead, if the top surface of the domain is rigid but allows slip, a favorable pressure gradient develops in the streamwise direction, causing the freestream to accelerate significantly. This happens because even when the top wall of the channel is set to allow slip, it still permits no through flow. There is always some small but finite vertical velocity above a flat plate in an infinite domain, even very far from the plate. This vertical velocity can be calculated from the Blasius solution as

$$V = \sqrt{\frac{\nu U_\infty}{2x}}\left(\eta f' - f\right) \tag{2.4}$$

where

$$\eta = y\sqrt{\frac{U_\infty}{2\nu x}} \tag{2.5}$$

is the similarity variable for the Blasius solution, $V$ is the vertical velocity, and $\nu$ is the kinematic viscosity. Here $x$ is the streamwise distance from the leading edge of the flat plate, $f$ is the streamfunction normalized by $\sqrt{2\nu U_\infty x}$, and $f' = \partial f / \partial \eta$.

Note that as $\eta$ becomes large, $f' \to 1$, and $(\eta - f) \to 1.21678$ (for more details, see White (1991)), so this equation reduces to

$$V = 0.86039\sqrt{\frac{\nu U_\infty}{x}} \tag{2.6}$$

Thus in order to model the boundary layer, it was necessary to simulate this vertical velocity. The top wall of the channel cannot be modified to allow through flow, so a different type of immersed boundary was placed below the top channel wall to force a suitable upflow. This "suction wall" forces the vertical velocity at each point to be that predicted by the Blasius solution (Eq. 2.6), thus allowing normal streamwise growth of the boundary layer. Unlike the solid-wall immersed boundaries, the suction wall only applies the body force in the vertical direction; it exerts no force in the spanwise or streamwise directions. This suction wall serves the same purpose as a small variation in area in a real wind tunnel, which is used to maintain a zero pressure gradient in a test section. The boundary layer can be made to grow as if from the leading edge of the plate (the plate starts at or near the end of the buffer zone) or the velocity can be set in the buffer zone to a Blasius profile for a given x-location on the plate. In either case the profile will develop correctly downstream.

A schematic diagram in Figure 2.1 shows the locations of the buffer zone, the suction wall, and the flat plate virtual surface. In the top image the y-direction is exaggerated by ten times compared to the x-direction, but with this scaling in mind, the dimensions are otherwise correct. The size of the buffer zone with respect to the size of the domain, the location of the suction wall in the domain, and the shape of the velocity profile displayed are all accurate (after accounting for the exaggeration in the y-direction). The bottom image is a close-up of the region where the edge of the buffer zone intersects the virtual surface, and the small region of unforced flow between the virtual surface and the bottom edge of the domain can also be seen. Note that although the virtual plate (shown as a thin black line) can only be seen in the bottom image, in fact it extends throughout the domain, lying just above the lower edge of the domain. The bottom image in Fig. 2.1 is for a flat plate case, but it would be identical for a textured

case (schematics with textures are shown later) because the textures do not begin until well downstream of the buffer zone, and the virtual surface remains flat until then.

The exact placement of the suction wall in the domain was originally determined by trial and error. The suction wall does not extend from one end of the channel all the way to the other; if it did the fluid which is sucked through and up would have no place to go. Instead, it extends from the middle of the buffer zone (point A in Fig. 2.1) to the end of the domain (point C). The portion of the suction wall which lies inside the buffer zone (between points A and B) is set to force a vertical velocity of zero (the same as the buffer zone is set to force) so there is no conflict between them. Since the suction wall is far from the boundary layer edge, the streamwise velocity within the buffer zone both immediately below the suction wall (region I in the figure) and between the suction wall and the slip-wall boundary at the top of the domain (region II) is forced to zero by the buffer zone body forces. The vertical velocity is forced to zero in these two regions. Outside the buffer zone, the suction wall draws fluid from the main part of the domain into the region between the suction wall and the top boundary (region III). Due to conservation of mass, the streamwise velocity above the suction wall increases along the length of the domain. Finally, the suction wall ends at the right edge of the domain (point C) (which, by the periodic nature of the domain, means it ends at the beginning of the buffer zone on the left edge) and a jet of fluid exits into the buffer zone. Another advantage of the Gaussian profiles of the α and β gains in the buffer zone (with the integral term present only in the central region) is that this jet can be slowly remixed with the flow from the rest of the domain, without any large-scale feedback into the region of interest (the area well below the suction wall, to the right of the buffer zone, and above the flat or textured virtual surface, region IV in the figure). This jet is also the reason the suction wall must begin in the middle of the buffer zone. The requirement that

streamwise velocity equal $U_\infty$ in region II, coupled with the addition of mass to the jet along the length of the domain (between points B and C), leads to a very high pressure in region II. The velocity gain term ($\beta$) alone is not strong enough to force the streamwise velocity to $U_\infty$, and thus the suction wall must begin in the region where the integral gain term ($\alpha$) is active.
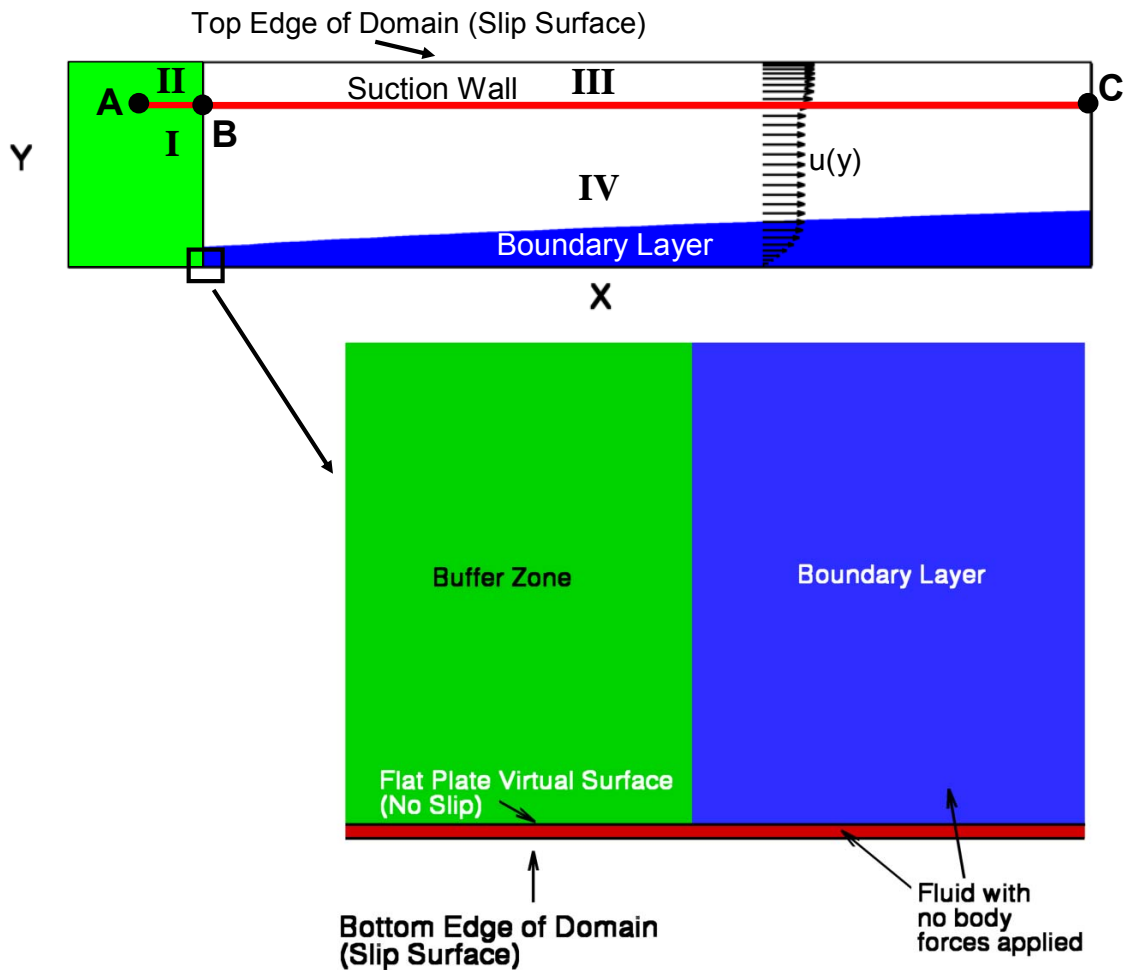


Figure 2.1:  Schematic of computational domain with buffer zone and suction wall employed to model a Blasius boundary layer. Top image shows entire domain, and is stretched in the y-direction but is otherwise to scale. Bottom images shows the virtual flat plate, and the small area of fluid beneath it.

**SURFACE TEXTURES EXAMINED**

So far spots have been examined over four surfaces: a flat wall, riblets, fins, and spanwise damping "fins". Both the riblets and fins are solid, no-slip surfaces created with the immersed boundary method. The fins are simple; they are only one grid node wide, and the only parameters of interest are their height and their spacing. Figure 2.2 shows the how the immersed boundary method is used to create the fins. Body forces are used to bring all three velocity components as close to zero as possible on the frozen grid points, which make up both the fins and the flat wall between them. No body forces are applied below the wall. As can be seen from the red and blue regions, the velocity is brought very close to zero on the fins. The method cannot quite recreate the sharp corner where the fins meet the flat wall, but this is unimportant.
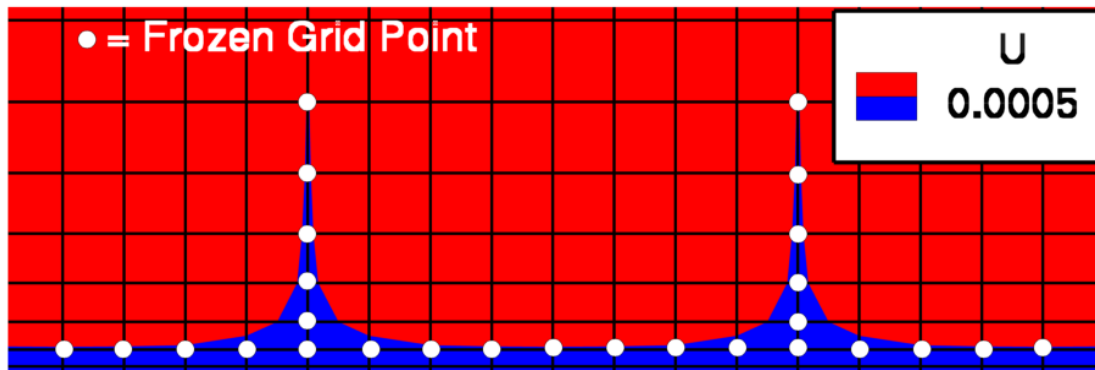


Figure 2.2:  Schematic view of two fins created with the immersed boundary method. Regions where streamwise velocity is above (red) and below (blue) 0.0005 $U_\infty$ are shown. The graphics package Tecplot performs linear interpolation in order to calculate velocity between between grid nodes.

The riblets are somewhat more complex due to the cosine grid in the normal direction. Also, since the body forces are applied at the grid nodes, the riblets are slightly stairstepped rather than completely smooth. If a sufficiently high resolution is used (so that each riblet is at least 5 or 6 grid nodes high) this stairstepping is not a problem.

Figure 2.3 shows which grid nodes are frozen to create the riblets. For more detail on how the various immersed boundaries are created, see Goldstein et al. (1995).
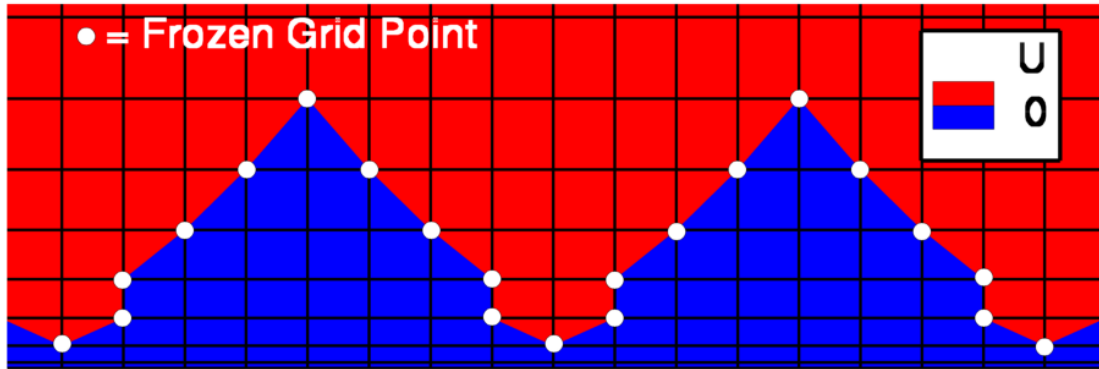


Figure 2.3:   Schematic view of two riblets created with the immersed boundary method. Regions where streamwise velocity is above (red) and below (blue) zero are shown. Tecplot performs linear interpolation in order to calculate velocity between between grid nodes.

The spanwise damping fins do not bring the flow to rest. Instead they only apply forces in the spanwise direction, and only the spanwise component of the velocity is forced to zero. Also note that for a given spacing and height the spanwise-damping fins occupy the same space as the regular fins, only the forces applied to the flow are different.

As discussed earlier, the textures do not begin immediately downstream of the buffer zone. In all of the spanwise damping fin cases and in the smallest riblet case and the smallest real fin case the textures begin 0.363 L from the left edge of the domain. (L is the total length of the domain in the streamwise direction. For reference, the buffer zone ends at 0.124 L.) After they begin, the textures ramp up to their full height over a distance of 0.01 L. In all of the other riblet and real fin cases the textures begin at 0.311 L, and ramp up over a distance of 0.06 L. In all cases, the textures reach their full height at 0.374 L.

Figure 2.2 is a schematic for the riblet case, and Figure 2.3 is a similar schematic for the fin case. So that they can easily be seen, the riblets and fins used in these two schematics have heights and spacings about three times that of the largest textures used in the actual runs. Other than this, the figure is to scale. The length of the ramp here is 0.06 L, corresponding to the ramp length for the larger riblet and fin cases. The buffer zone and the perturbation are shown in their correct locations. The perturbation will be discussed later in this chapter. Only the section of the domain near the bottom wall is shown; the suction wall is located well above the visible area.
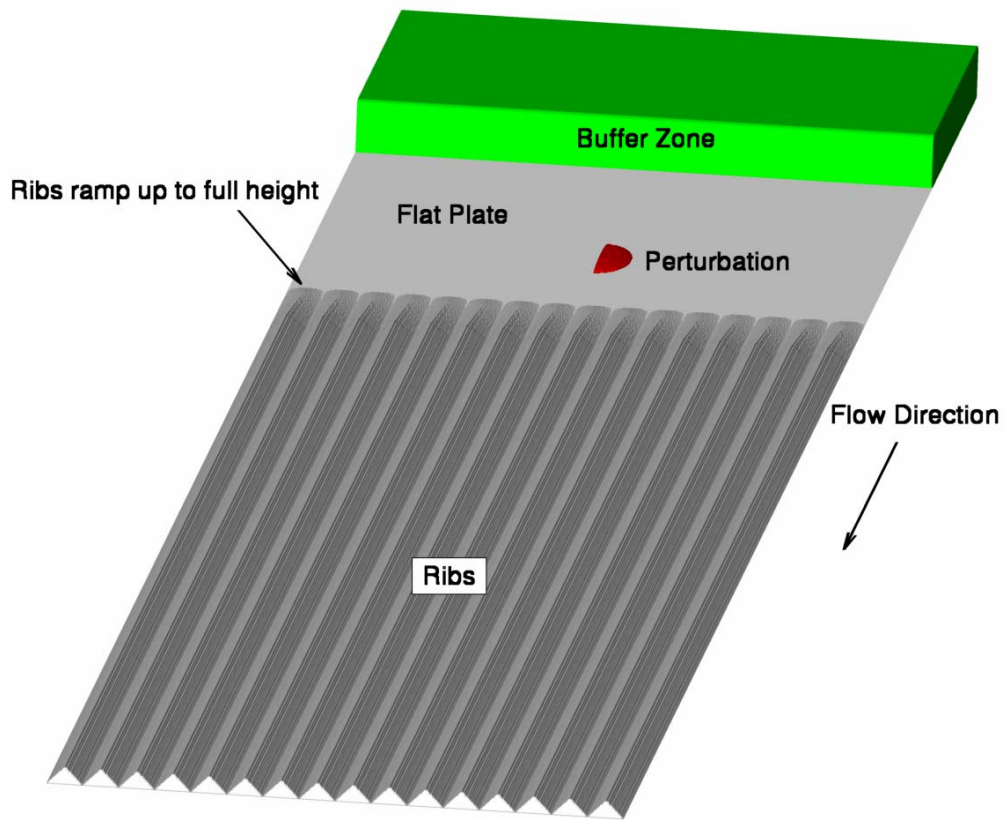
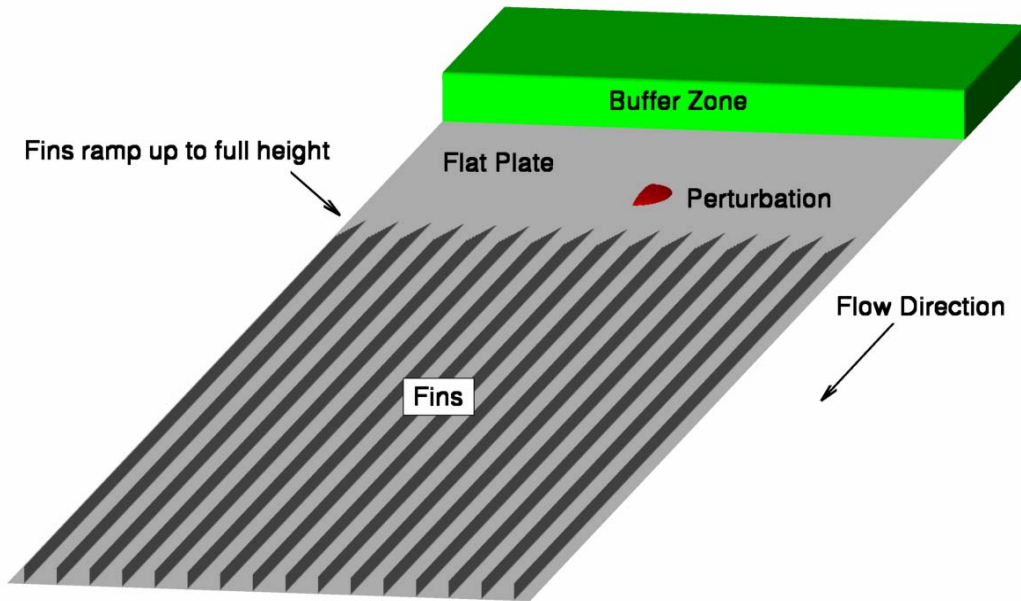Figure 2.2: Schematic for riblet case showing 16 riblets, the region of the perturbation, and the buffer zone.

Figure 2.3: Schematic for the fin case showing 8 fins, the region of the perturbation, and the buffer zone.

**INITIAL PERTURBATION**

The size and shape of the perturbation was determined by trial and error. As found by Wygnanski (1976, 1982), if the flow is not perturbed strongly enough no spot will develop. The perturbation used for the results presented in this report was a bump on the top of the flat plate, in the region between the end of the buffer zone and the beginning of the textures. The bump is a solid surface created with the same immersed boundary technique as the plate and the textures. It is made to appear at the beginning of the simulation, and is then removed after a brief time ($0.012\ T_{tot}$, where $T_{tot}$ is the total length of the run). The shape of the bump is determined by the equation

$$R = \sqrt{((y - y_{wall})^2 + (z - 0.5W)^2 (1.0/30.0) + (x - x_{mid})^2 (1.0/100.0))} \qquad (2.7)$$

where $x_{mid}$ is the midpoint of the perturbation in the streamwise direction (located at 0.249 L, where L is the length of the domain in the streamwise direction), $y_{wall}$ is the y-

19

location of the flat plate, and W is the width of the domain in the spanwise direction. The perturbation encompases the grid nodes for which $R \leq 0.10$ and which lie on the left side of the spanwise centerline (where $z - 0.5W \leq 0$). The bump is deliberately made asymmetric about the spanwise centerline in order to keep the spot from developing perfect left-right symmetry. Slight variations in the initial perturbation are used to generate differing spots over a given surface texture for the purposes of ensemble averaging (see below).

### ENSEMBLE AVERAGING

The growth and spreading of turbulent spots is a chaotic process and thus the detailed structure of a spot can be highly sensitive to small variations in the size and shape of the perturbation which triggers it, among other things. Past experimenters such as Wygnanski et al. (1976) used ensemble averaging to generate the profile of a "typical" spot. Multiple spots are run with the same setup, and results of the these runs are averaged in some way to determine the ensemble averaged profile. In most DNS studies of spots performed to date, however, the significant computational expense associated with simulating spots has prevented the use of ensemble averaging.

When comparing textures to one another it is especially important to separate changes to the spot growth caused by the textures from random variations in spot growth due to other factors. For example, the spot will grow at least slightly differently if the centroid of the perturbation is directly upstream of a riblet valley than it would if the centroid of the perturbation were directly upstream of a riblet crest. It is therefore difficult to ascertain the effects of various surface textures on spot growth by means of comparing a single spot over each set of textures with a single spot over a flat plate.

Within the limits of available computational resources, an attempt was made in this work to obtain ensemble averaged spots over the flat plate and over each of the real textures which was examined. Four different spots were simulated for each case; the differences between the spots were the results of slight variations in the initial perturbation. The four perturbation shapes are shown in Figure 2.4. Note that for each case (the flat wall, or a specific textured surface) the spot generated by the first perturbation is referred to in the rest of this work as "Spot 1", the spot generated by the second perturbation is "Spot 2", etc. Equation 2.7 describes the shape of the first perturbation. The others are simply the same shape with one or both ends cut off, as shown in the figure.

The flowfields of the four runs for each case were then averaged at each output time interval to obtain the "ensemble averaged spot". So, for example, at any given grid node at a particular output interval,

$$u_{avg} = \frac{\left(u_{run1} + u_{run2} + u_{run3} + u_{run4}\right)}{4} \tag{2.8}$$

and similarly for all the other flow quantities discussed in this work (v, w, $\omega_x$, $\omega_y$, $\omega_z$, enstropy, and $\lambda_2$). It is important to understand the results of applying this simple averaging procedure to variables that depend on other flow variables in a nonlinear way. The enstrophy, for example, is the magnitude of the vorticity vector. It is given by the equation

$$ens = \sqrt{\omega_x{}^2 + \omega_y{}^2 + \omega_z{}^2} \tag{2.9}$$

and thus it depends on the components of the vorticity vector in a nonlinear way. What this means is that calculating the enstrophy (at a given grid point and time) in each of the four runs and arithmetically averaging the four values in the manner of Eq. 2.8 does not give the same value as would be obtained by arithemetically averaging the values of the

vorticity components, and then using those average values in Eq. 2.9. In equation form, the previous sentence means that

$$\text{ens}_{\text{avg}} = \frac{\left(\text{ens}_{\text{run1}} + \text{ens}_{\text{run2}} + \text{ens}_{\text{run3}} + \text{ens}_{\text{run4}}\right)}{4} \neq \sqrt{\omega_{\text{x,avg}}^2 + \omega_{\text{y,avg}}^2 + \omega_{\text{z,avg}}^2} . (2.10)$$

In the same way, calculating the arithmetic average of $\lambda_2$ for the four runs does not give the same value as calculating $\lambda_2$ directly from the ensemble averaged flowfield.
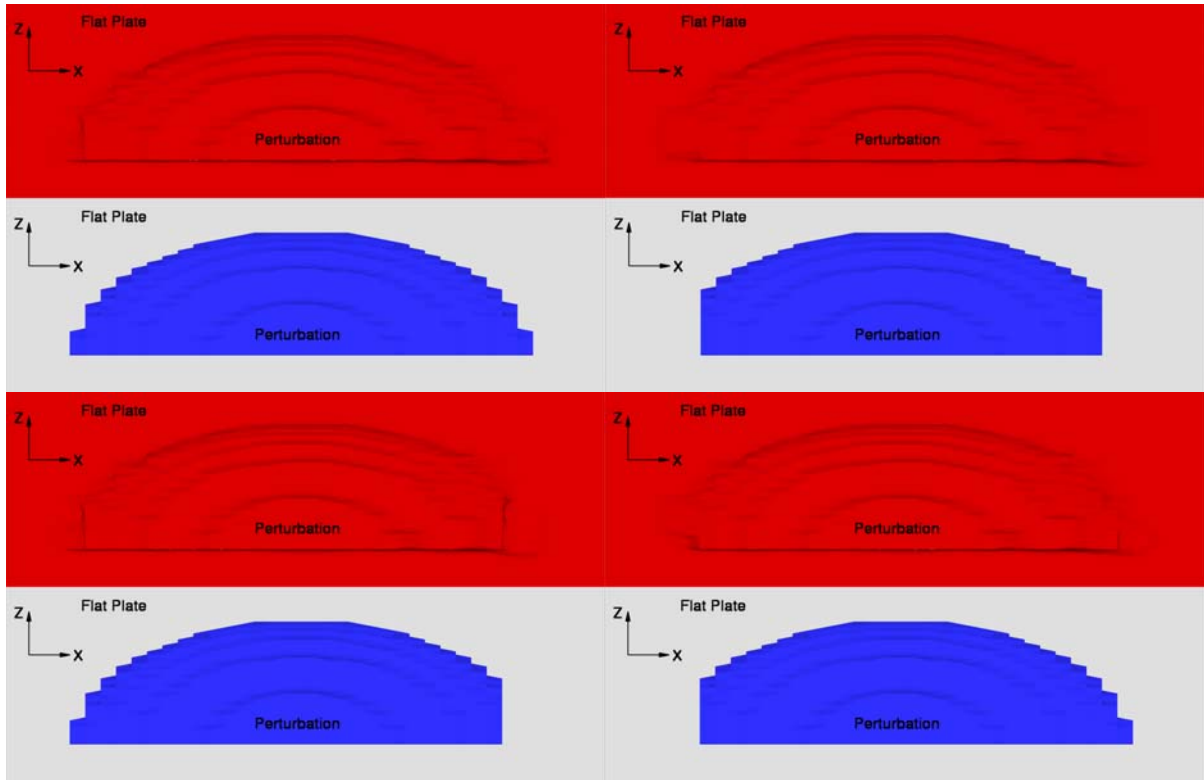


Figure 2.4:  Top left is the perturbation for Spot 1, top right is perturbation for Spot 2, bottom left is perturbation for Spot 3, and bottom right is perturbation for Spot 4. In each picture, the top image shows an isosurface of streamwise velocity at the value of 0.01 $U_\infty$ just before the perturbation is removed, and the bottom image shows the shape of the perturbation based on which grid nodes are frozen.

When the code is run from a cold start the streamwise velocity everywhere along the plate is initialized to that of the Blasius profile *for a single x-location*. It is not possible to incorporate the vertical velocity from the Blasius solution, since the top wall of the channel is no-through-flow, and the steady-state velocity profile above the suction wall is not known initially. The spanwise velocity is zero for a Blasius boundary layer. Thus, since the code must satisfy continuity at every time step, initially there can be no variation of streamwise velocity with distance along the plate. It therefore takes a significant amount of time (several flow through times) for a steady state, spatially developing boundary layer to emerge. It is this relaxed profile which provides the initial conditions for the turbulent spot simulations.

In the past this relaxation was performed on the same domain and with the same grid resolution as the spot simulations (Strand and Goldstein, 2006), and thus the process took a significant amount of computational time (longer than the simulation of the actual spot). For the current work a method was devised which significantly reduced the time required for relaxation. The domain is always periodic in the spanwise direction, and all of the textures examined here are evenly spaced. Although the flowfield over an individual texture (an individual riblet or fin) is 3-dimensional, this flowfield is identical for each texture on the surface. Therefore, for a given textured surface, the relaxation can be performed on a domain which has the same streamwise length as the domain for the full spot simulation, but which is only as wide as the crest-to-crest texture spacing. In the riblet case, this reduced domain encompasses one entire riblet. In the fin case, the reduced domain has the fin on the centerline, and on either side of the fin the domain extends halfway to where the next fin would be located. The flow is allowed to relax to a steady state on this reduced domain, and the flowfield for the full domain is generated by

simply cloning this flowfield (side by side) as many times as necessary to reach the desired domain width for the spot simulation. Flowfields generated with this method were found to be identical to those generated by performing the relaxation on the full domain. In practice, because of the fact that the texture shapes (which grid nodes are frozen) are defined on the 3/2 grid (see Kim et al. (1987) and Handler et al. (1989) for discussion of the 3/2 grid) but the expansion from the reduced to the full domain takes place on the regular grid, the reduced domain is usually made wide enough to accommodate two or three individual riblets or fins, instead of just one. Performing the relaxation with the reduced domain cuts the time required for relaxation by an order of magnitude, so that the great majority of computational time is spent simulating the spots instead of preparing the initial laminar steady-state flowfield over the textured surfaces.

### BLASIUS PROFILE VERIFICATION

Initially, it was necessary to verify that the suction wall method permitted proper spatial development of the boundary layer. In order to check that the boundary layer was growing properly, profiles were examined for several downstream locations and compared to the Blasius solution. Figure 2.4 shows the boundary layer profile at the midpoint of the domain in the streamwise direction. The flow is completely uniform in the spanwise direction. The profile corresponds to a position along the plate which is $54.57\delta$ from the leading edge, where $\delta$ is the boundary layer 99% thickness at the streamwise location of the profile shown. Both the streamwise and wall-normal velocity components are shown in the figure, and both compare well with the Blasius solution.
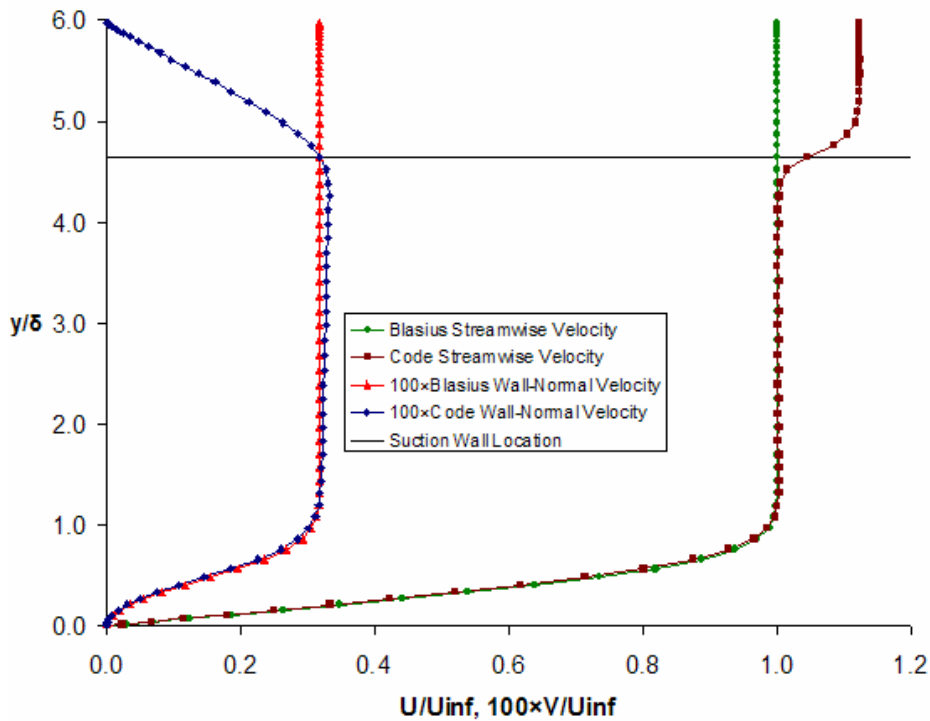
Figure 2.5: Comparison of the boundary layer profile developed with the suction wall method to that predicted by the Blasius solution midway down the plate. Note that the simulated vertical velocity agrees with the Blasius value at the suction wall location.

## GRID CONVERGENCE

It is very difficult to establish grid convergence for these types of simulations. The growth of a turbulent spot is a chaotic process, and thus the final detailed structure of the spot is highly sensitive to the initial perturbation and to the exact texture shapes. Even in the case of spots over a flat wall, tiny differences in the eddy structure between two similar spots will be magnified over time, and after the spots have propogated a significant distance downstream they will appear completely different at the finest scales. This is seen in Chapter 4, where spots over the same surface have differences in spreading angle due to slight variations in the initial perturbation.

As discussed in previous sections, the body forces that create the immersed boundaries (flat plate, textures, perturbation, buffer zone, and suction wall) are applied at the grid nodes. Even if the grid resolution is more than adequate to model the flowfield, simulations with different resolutions will still have slight differences in the body force field which is applied to generate the textures. Thus, even with vast computational resources (memory and processor time), it would be nearly impossible to demonstrate grid convergence by comparing the exact eddy structure of spots simulated with different grid resolutions. Instead, the demonstration of grid convergence would require ensemble averaging. If the grid is completely converged, the ensemble averaged spot flowfield should be nearly identical after the grid resolution is increased.

The investigation of grid convergence performed so far has been limited by both computational time and memory constraints. Available computational time has prevented the use of ensemble averaging for grid convergence testing. Due to memory constraints it was not possible to significantly increase the grid resolution while still using the same domain as that used for the spot simulations presented later in this work (see Chapter 3 for details on the domain and grid used for these simulations). However, by cutting the domain length in half, it was possible to use half as many grid points while still retaining the same grid resolution. Thus, on this half-length domain, sufficient memory was available to double the grid resolution in the streamwise (x), wall-normal (y), or spanwise (z) directions.

This alone does not solve the problem, because the smallest scale turbulent eddies will occur where $Re_x$ is highest (and the spot has grown largest), near the end of the streamwise domain. If the domain were simply cut in half and the fluid properties left unchanged, $Re_x$ would be roughly ½ as large at the end of the shortened domain, and thus the fine scale turbulence would be easier to resolve than it would be for the full domain.

To account for this the kinematic viscosity of the simulated fluid is cut in half for the half-length domain runs, and thus $Re_x$ at the end of the half-length domain is similar to that at the end of the full domain. They are not exactly equal because in the half-length domain case the velocity profile forced by the buffer zone corresponds to the Blasius profile at a location farther from the plate leading edge than in the full-domain case. (Remember that the Blasius profile forced in the buffer zone corresponds to a specific x-location on a flat plate; this x-location is unrelated to the size of the computational domain, and can be set as desired). This was done intentionally so that Rex would be slightly higher for the half-length domain cases. $Re_x$ was equal to 223,520 at the end of the half-length domain, which is slightly more than the $Re_x$ of 198,219 at the end of the full domain.

In the full-domain spot simulations the shape of the perturbation is given by Eq. 2.7. Since all of these runs are at the same resolution it is not a problem that the actual shape of the perturbation is stairstepped rather than smooth (since the body forces are applied at the grid nodes). For the runs where grid convergence is being investigated, however, this stairstepping will be a problem, because the goal is to simulate the exact same flowfield with two different resolutions. The stairstepping would of course be different with different resolutions, and thus a perturbation shape that does not require stairstepping must be used. To this end, the grid convergence runs use the perturbation shown in Fig. 2.6. This perturbation keeps the necessary feature of spanwise asymmetry, without the need for stairstepping. The shape of the perturbation is set such that doubling the grid in any direction does not alter the size or shape of the perturbation.

With the domain and perturbation set, four cases were run with the shortened domain: one with the same grid resolution as the full-domain spot runs, one with double the resolution in the streamwise direction, one with double the resolution in the wall-

normal direction, and one with double the resolution in the spanwise direction. The results of these runs are shown in Fig. 2.7 and Fig. 2.8. Figure 2.7 has a zoomed in top-down view of each spot. It can easily be seen that the detailed eddy structure of the spots is not the same, and in fact they are not even exactly the same shape. However, they are all roughly the same size, and all have the same overall arrowhead shape. All four spots also move downstream at the same speed, and have the same streamwise extent. Figure 2.8 shows the growth of each spot as it propogates downstream. All four images look quite similar, and it seems that although the spot shapes at any given instant are not identical, the overall spot growth is comparable in all four cases. To quantify this somewhat, the maximum difference in the final spot half-width between any two cases is only 4.4%. For the details on calculation of the spot half-width, see Chapter 4. With this in mind, it seems reasonable to conclude that although the grid is not sufficiently resolved to produce identically shaped spots (and due to the chaotic nature of spot growth this might never be practically possible), it is sufficiently resolved for purposes of examining spot growth and spreading.
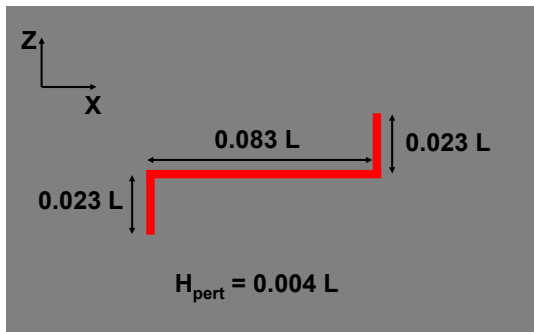


Figure 2.6: Perturbation shape used for the grid convergence runs on the half-length domain. Perturbation extends upward from the flat plate. Hpert is the perturbation height and L is the length of the domain in the streamwise direction.
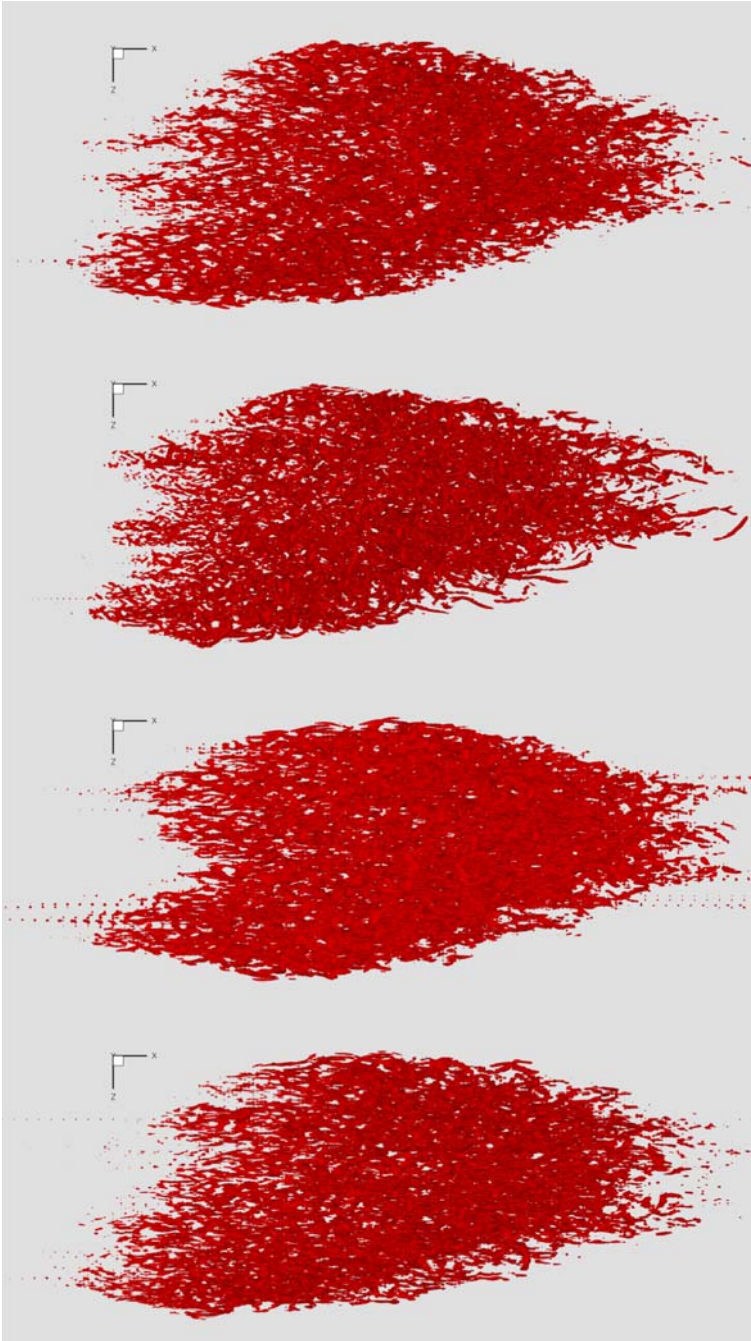
28

Figure 2.7: Closeup views of turbulent spots over a flat wall. Spots are shown at the same time step and drawn with an isosurface of $\lambda_2$ at the value of $-0.0071$ $(U_\infty/\delta_o^*)^2$. From the top, the images are of the case with the same grid resolution as the full-domain spot simulations, and with double the grid resolution in the streamwise direction, wall-normal direction, and spanwise direction, respectively.
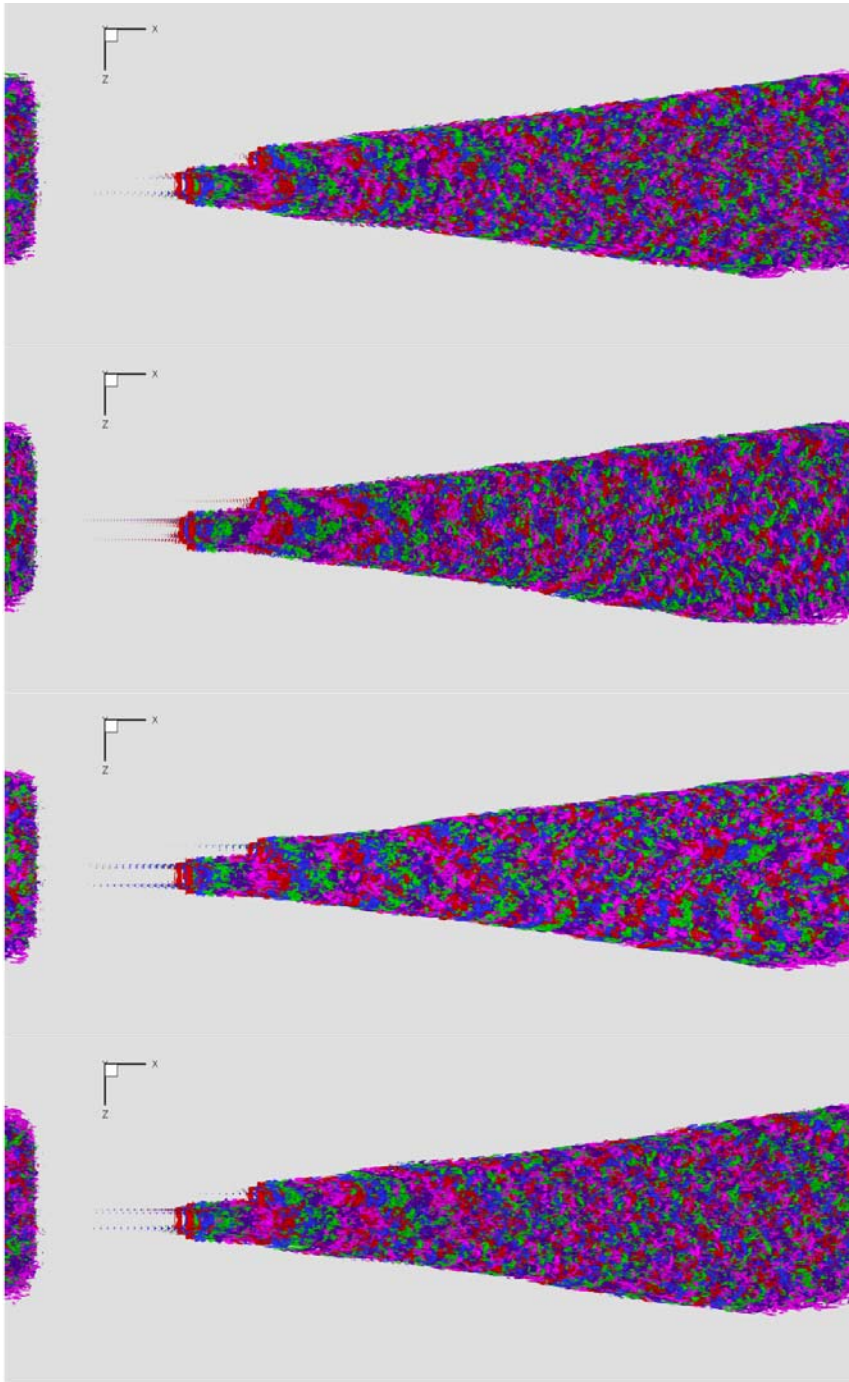
Figure 2.8:  Top view of spot growth over a flat wall.  Images are in the same order as in Fig. 2.7.  For each case, isosurfaces of $\lambda_2$ at the value of -0.0071 $(U_\infty/\delta_o^*)^2$ for all output time steps are shown together to illustrate spot growth.

# Chapter 3:  Qualitative Results

**FLAT WALL SPOT**

Before the effects of surface textures on spots are investigated, it is useful to examine spots over a flat plate.  This provides a basis for comparison both with the surface texture runs presented later, and with the experiments, simulations, and flow visualization found in prior works (such as those described in Sect. 1).

The domain used for these simulations (and all others presented in this chapter) had dimensions of 530.7 $\delta_o^*$, 21.2 $\delta_o^*$, and 106.1 $\delta_o^*$ in the streamwise (x), wall-normal (y), and spanwise (z) directions respectively, where $\delta_o^*$ is the boundary layer displacement thickness at the location of the perturbation, as calculated from the Blasius solution.  For this domain, 512×64×512 spectral modes were used in the x, y, and z directions, respectively.  The perturbation was introduced at t = 0 and remained in the flow until t = 7.88 $\delta_o^*/U_\infty$.  The simulation continued until t = 636.8 $\delta_o^*/U_\infty$, by which time much of the spot had passed the end of the streamwise domain (and entered the buffer zone).  The Reynolds number based on displacement thickness, $Re_{\delta*}$, was 376.8 at the perturbation location.  $Re_x$ at the end of the streamwise domain was 198219.

A top-down view of the flat-wall spot at times $t_1$ = 159.1 $\delta_o^*/U_\infty$, $t_2$ = 318.4 $\delta_o^*/U_\infty$, and $t_3$ = 477.6 $\delta_o^*/U_\infty$ is shown in Fig. 3.1.  The spot is drawn with isosurfaces of $|\omega_x|$ at the value of 0.236 $U_\infty/\delta_o^*$.  As the spot matures, it takes on the expected arrowhead shape.  It is asymmetric about the spanwise centerline since the perturbation itself is asymmetric.  This was done intentionally, in order to prevent the spot from developing with perfect spanwise symmetry since experimental spots do not have perfect left/right symmetry.  Perfect symmetry leads to some unrealistic results, such as zero normal and streamwise vorticity, zero spanwise velocity, and zero helicity on the spot centerline.  A

31

quick glance at the figure indicates that the leading edge is moving at a fairly constant speed, since the leading edge moves about the same distance between $t_1$ and $t_2$ as it does between $t_2$ and $t_3$.
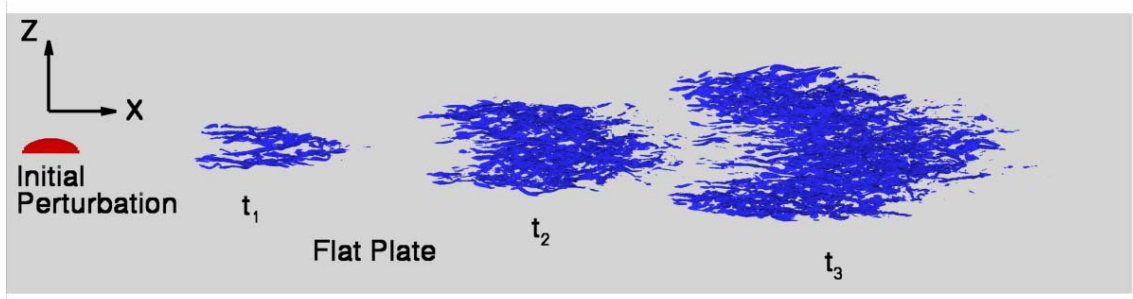


Figure 3.1:  Top view of a turbulent spot over a flat wall, drawn with isosurfaces of $|\omega_x|$ at the value of 0.236 $U_\infty/\delta_o^*$ and shown at $t_1 = 159.1\ \delta_o^*/U_\infty$, $t_2 = 318.4\ \delta_o^*/U_\infty$, and $t_3 = 477.6\ \delta_o^*/U_\infty$.  Resolution was 512×64×512 spectral modes in the x, y, and z directions, respectively.
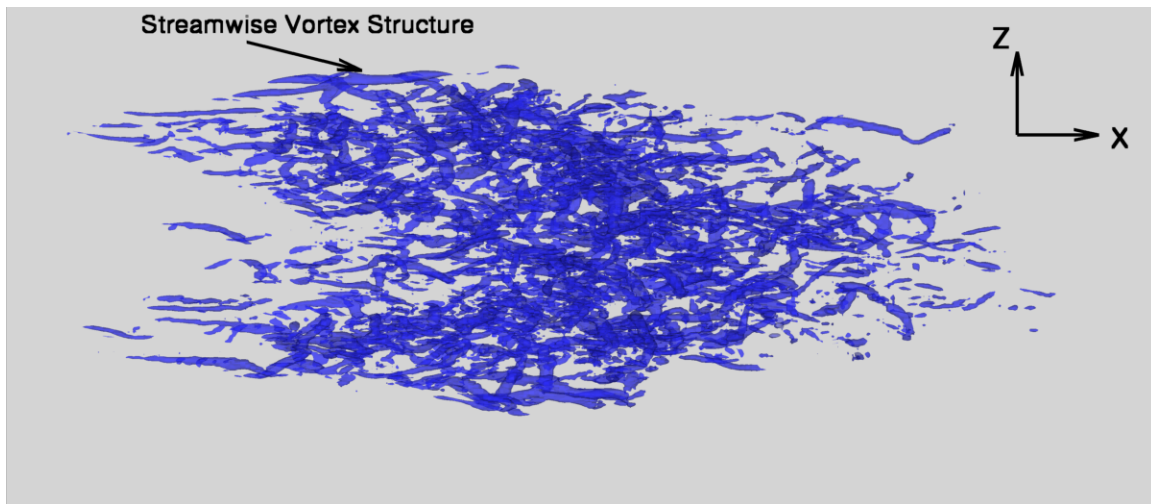


Figure 3.2:  Closeup view of a turbulent spot over a flat wall, drawn with an isosurface of $\lambda_2$ at the value of 0.0071 $(U_\infty/\delta_o^*)^2$, and shown at $t = 398.0\ \delta_o^*/U_\infty$.

Figure 3.2 shows a closeup view of the same spot at a slighly different time, this time using an isosurface of the swirling strength, $\lambda_2$.  The swirling strength is useful for picking out vortex cores.  Note the long streamwise vortical structures, especially near

32

the edge of the spot. Figure 3.3 is a flow visualization photograph of a turbulent spot in water, with $Re_x$ = 200,000 in the center of the spot (as compared to 138,000 for the spot shown in Fig. 3.2). The two spots are very similar in shape, especially near the wingtips and at the rear, where long streamwise structures are clearly visible in both. The front tip of the spot is slightly sharper in Fig. 3.3, most likely because $Re_x$ is somewhat higher for that spot, and spots tend to be more clearly defined at higher $Re_x$. This can be seen in several other flow visualization pictures from Van Dyke (1982), which was also the source for Fig. 3.3.
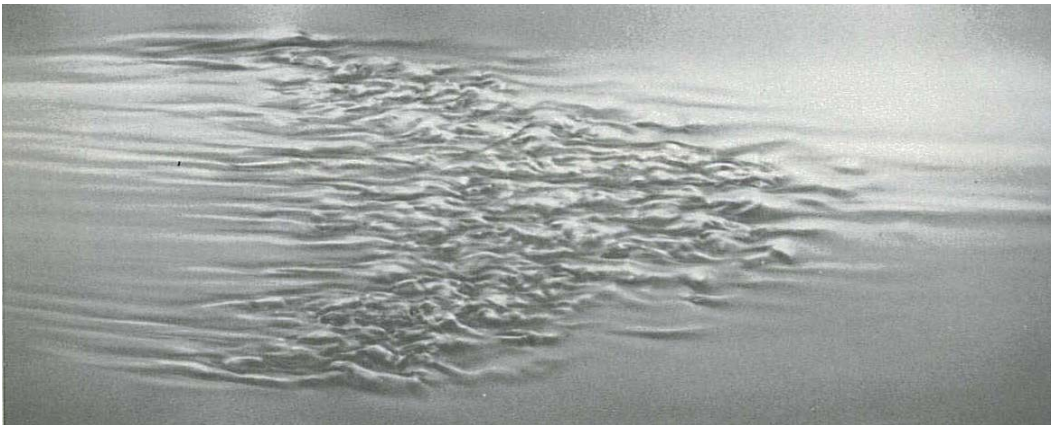


Figure 3.3:  Top-down view of a turbulent spot over a flat plate, visualized with aluminum flakes in water. Image by Cantwell, Coles, and Dimotakis, taken from *An Album of Fluid Motion*, by Milton Van Dyke. $Re_x$ = 200,000 in the center of the spot.

Figure 3.4 shows a close-up side view of the same flat wall spot. The overhang found by prior experiments and DNS simulations is clearly visible near the leading edge of the spot. Note also that the spot remains significantly below the suction wall, and thus the body forces imposed by the suction wall are unlikely to affect the spot directly.

Schubauer and Klebanoff (1956) argued that the height of the spot can be estimated by the thickness of a hypothetical turbulent boundary layer which originates at the location of the perturbation, and which has an initial thickness equal to that of the

laminar boundary layer at the perturbation. The data of Wygnanski et al. (1982) also support this idea. In Figure 3.5, isosurfaces of $|\omega_x|$ at the value of $0.188\ U_\infty/\delta_o^*$ are shown for all output time intervals simultaneously (data output takes place at intervals of 15.9 $\delta_o^*/U_\infty$). Obviously the isosurfaces overlap and obscure one another. However, the point is only to see the variation in the peak height of the spot as it moves downstream. The hypothetical turbulent boundary layer thickness is shown on the figure as well, and is calculated from the equation

$$\delta_{turb,hypothetical} = \frac{0.16(x - x_{pert})^{6/7}\ \nu^{1/7}}{U_\infty^{1/7}} + \delta_{lam,pert} \qquad (3.1)$$

where $\delta_{lam,pert}$ is the laminar boundary layer thickness at the location of the perturbation (from the Blasius solution), $x_{pert}$ is the streamwise location of the perturbation, $U_\infty$ is the freestream velocity, and $\nu$ is the kinematic viscosity. The one-seventh power law expression used to describe the growth of the turbulent boundary layer was taken from White (1991). It is apparent from the figure that the height of the flat wall spot fits this approximation fairly well. This is a further indication that the suction wall is not having direct effects on the growth of the spot, and that the spot is growing properly as it moves downstream.
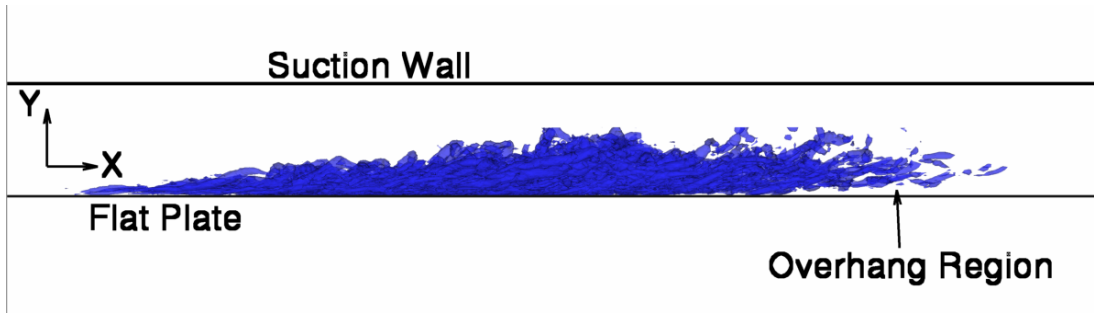
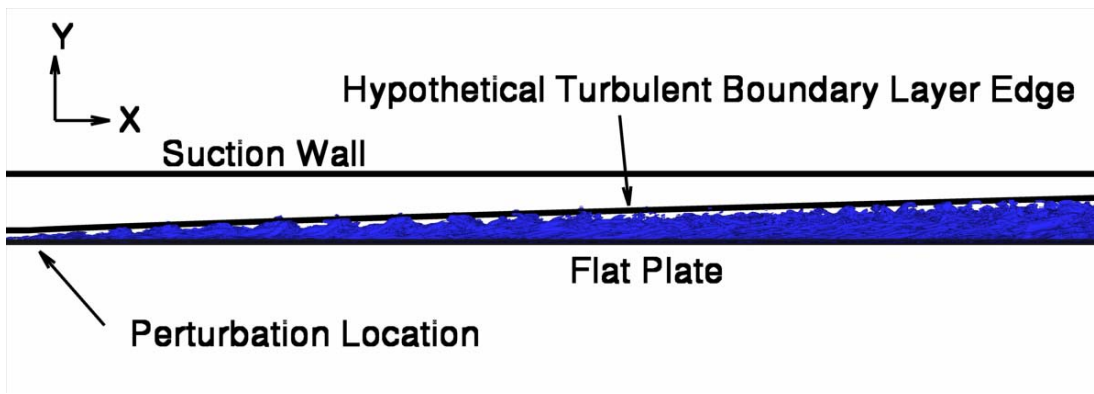Figure 3.4:   Side view of the spot in Fig. 3.2, at the same time, and shown with the same isosurface.



Figure 3.5:   Comparison of spot height with the thickness of a hypothetical turbulent boundary layer originating at the perturbation, with an initial height equal to the laminar boundary layer thickness at the perturbation.

Figure 3.6 is an oblique perspective view from the rear of the same spot. The usefulness of the swirling strength is apparent here; an isosurface of $\lambda_2$ clearly displays the multiple overlapping and entwined hairpin and streamwise vortical structures that make up the spot. One particular hairpin is labeled in the figure, but they are present throughout the spot. The structures are more complex and interwined in the spot center, and the hairpin legs do not necessarily align with the streamwise direction. Near the spot wingtips, both hairpins and other streamwise vortices are present. These other streamwise vortex structures appear to be the "quasi-streamwise vortices" described by

Singer (1996). In this figure and in several of the other spot figures shown so far the relaminarization of the flow after the passage of the spot is apparent, since there are no vortical structures present in the wake of the spot.
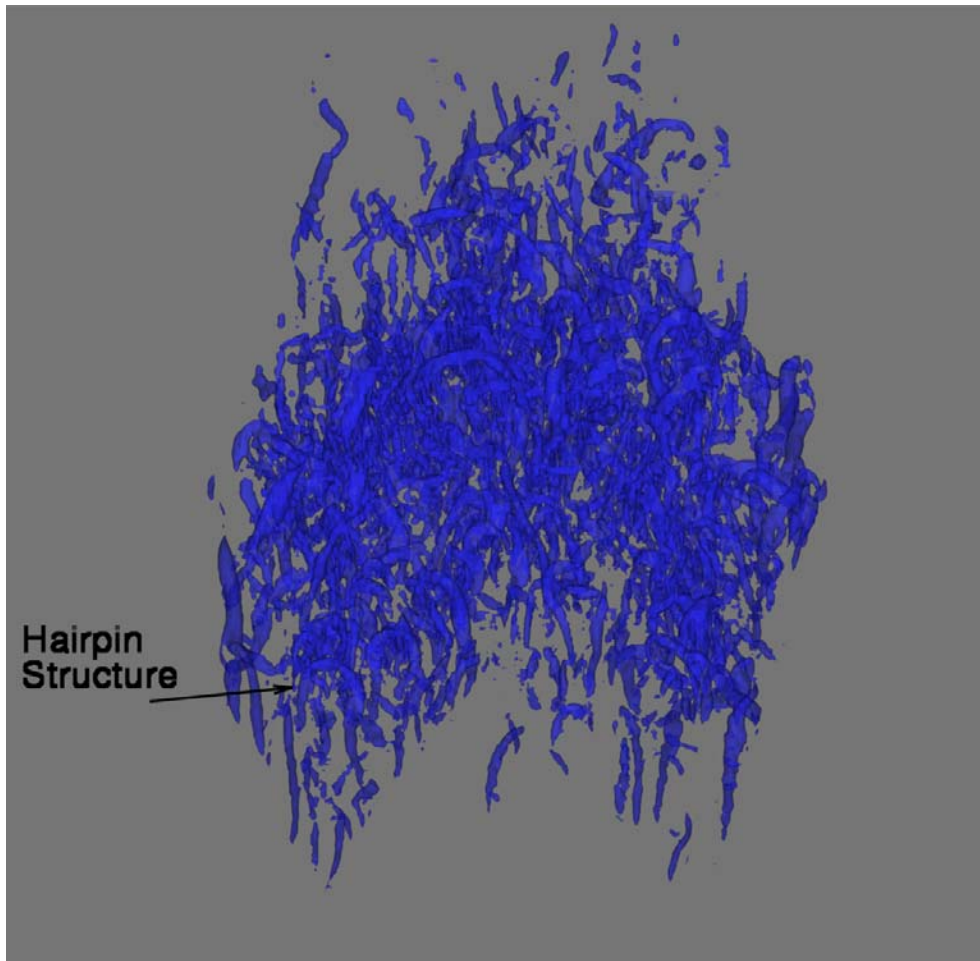


Figure 3.6:  Perspective view from the top rear of the spot. Viewer is 40° above the horizontal looking down toward the spot and facing downstream.

Figure 3.7 is a cross-section (a zy slice) of the same flat wall spot taken at t = 366.1 $\delta_o^*/U_\infty$ at a location 212.8 $\delta_o^*$ downstream of the perturbation. Note that the regions of greatest enstrophy are mostly concentrated near the wall. The prominent

mushroom-like structures are created when fluid erupts away from the wall due to the interaction of streamwise vortical structures with each other and with the wall.

It is apparent from Fig. 3.7 that the edges of the spot are relatively sharp, with a quick jump from turbulent to laminar flow. This seemed to be the case in the previous top-view figures as well, but in those images the spot was drawn with a specific isosurface of either $\lambda_2$ or $|\omega_x|$ (spots drawn with isosurfaces of enstrophy look very similar). It is conceivable that there could be regions extending beyond the apparent "edge" of the spot, where the values of $\lambda_2$ or $|\omega_x|$ are much higher than would be expected in a laminar boundary layer, but still below the value used for the isosurface. In that case, the spot might actually be significantly larger than it appears in the prior images. In a 2D slice such as Figure 3.7, however, continuously varying contours can be displayed, and the above problem is eliminated. There is clearly not a large region of semi-turbulent flow at the edges of the spot; instead the spot edge is fairly sharp. The topic of defining the spot edges will be discussed in great detail in Sect. 4.

Figure 3.8 is a photograph showing a cross-section of a spot over a flat plate in a wind tunnel, where smoke is used to visualize the spot. The same mushroom-like structures that are seen in Fig. 3.7 are also clearly visible here, and the ratio of spot width to spot height appears approximately the same. Even the number of large, distinct mushroom eddy structures is the same in both images (four in each), although this is probably coincidental (and also dependent on an individual's definition of "large" and "distinct").
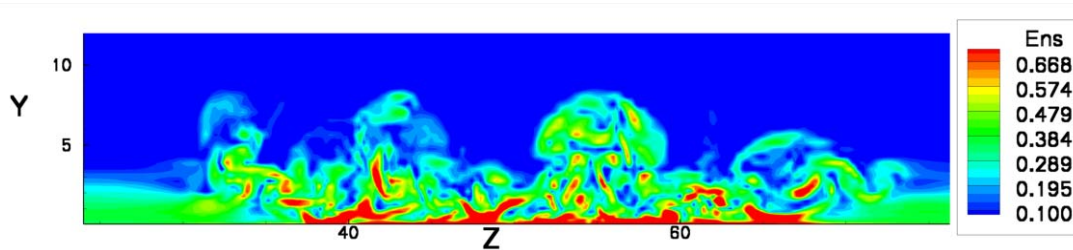
Figure 3.7:   Contours of enstrophy on a zy plane located 212.8 $\delta_o^*$ downstream of the perturbation, at time t = 366.1 $\delta_o^*/U_\infty$.  The y and z axes have units of $\delta_o^*$, and the units of enstrophy (shown in the contour legend) are $U_\infty/\delta_o^*$.



Figure 3.8:   Cross-section of a turbulent spot over a flat plate in a wind tunnel.  Smoke is used to visualize the spot.  Image by Perry, Lim, and Teh, taken from *An Album of Fluid Motion*, by Milton Van Dyke (1982).

### SPANWISE DAMPING FINS

As discussed in Sect. 2, spanwise damping fins occupy the same space in the domain as real fins, but they apply the immersed boundary body forces only in the spanwise direction.  The spanwise velocity is forced to be nearly zero on the fin, while the streamwise and wall-normal velocities are not directly affected.

Figure 3.9 shows results for the three spanwise damping fin cases.  The domain and perturbation were identical to that described previously for the flat wall case, and 512×64×512 spectral modes were again used in the x, y, and z directions, respectively.
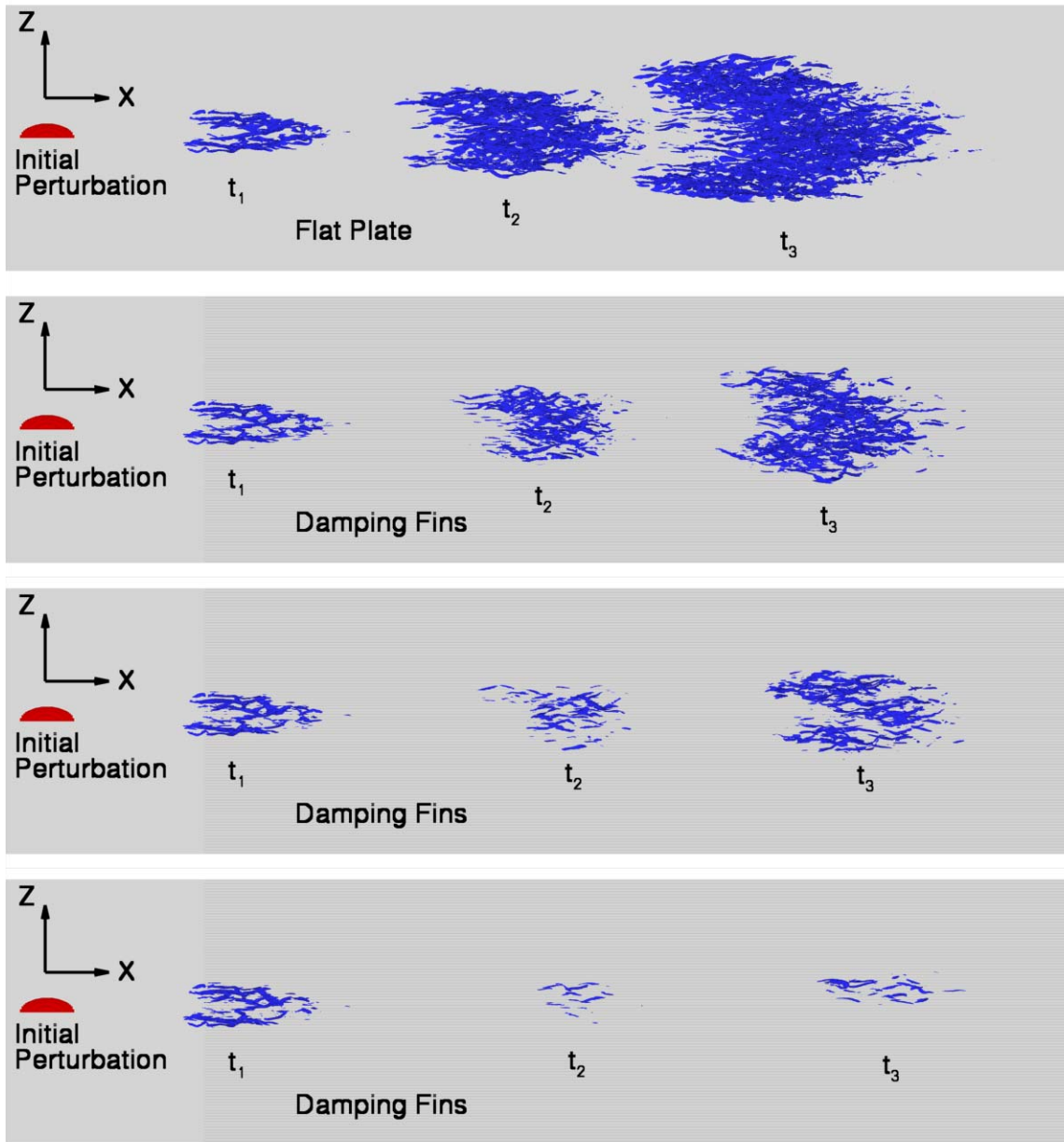
38

Figure 3.9: Top view of turbulent spots over a flat plate (the top image, which is the same as in Fig. 3.1) and damping fins (the next three images), drawn with isosurfaces of $|\omega_x|$ at the value of 0.236 $U_\infty/\delta_o^*$ and shown at $t_1 = 159.1$ $\delta_o^*/U_\infty$, $t_2 = 318.4$ $\delta_o^*/U_\infty$, and $t_3 = 477.6$ $\delta_o^*/U_\infty$. Fin height was 0.53 $\delta_o^*$, 0.80 $\delta_o^*$, and 1.06 $\delta_o^*$ for the top, middle, and bottom fin cases, respectively. In all three damping fin cases, fin spacing was 1.11 $\delta_o^*$.

39

Even with the shortest damping fins ($h = 0.53\ \delta_o^{*}$), the effect on the spot is significant. The lateral spreading of the spot is slightly decreased, and the streamwise length of the spot is decreased by a greater percentage. The strength of the turbulence inside the spot is clearly lessened as well, since fewer vortical structures can be seen, and they are less closely packed. These effects are all more prominent in the $h = 0.80\ \delta_o^{*}$ case. Finally, in the $h = 1.11\ \delta_o^{*}$ case, the spot is almost completely eliminated. It actually decreases in size (both lateral spread and streamwise length) between $t_1$ and $t_2$. Between $t_2$ and $t_3$, it lengthens, but its lateral spread decreases further. It is possible that were this spot to be followed further (in a longer domain, so it does not enter the buffer zone) it would disappear entirely, leaving completely laminar flow.

For each time shown in the figure, the front tip of the spot is at nearly the same streamwise location in the three damping fin cases as it is in the flat wall case, so clearly the damping fins have little or no effect on the velocity of the front tip of the spot. This is not unexpected, since they apply no forces in the streamwise direction, and there is no reason to expect that the front tip velocity would be affected by either spot size or lateral spread.

Figure 3.10 is a zy slice taken at a location $212.8\ \delta_o^{*}$ downstream of the perturbation at $t = 334.3\ \delta_o^{*}/U_\infty$, showing contours of enstrophy for the $h = 1.11\ \delta_o^{*}$ damping fin case. This figure is comparable to Fig. 3.7 for the flat wall case, except that it is taken two time intervals earlier (data output occurs at intervals of $15.9\ \delta_o^{*}/U_\infty$). The spot length is greatly decreased over the damping fins, so even though the front tip moves at the same speed, the spot passes through a given zy plane much quicker than in the flat wall case. Thus using the data at this streamwise location at the time interval shown in Fig. 3.7 misses most of the spot. Comparing this image to the one in Fig. 3.7, the smaller size of the spot over the damping fins is obvious. The contour levels are the same in both

40

figures, so simply comparing the amount of red in the two images makes it very clear that not only do the damping fins decrease the growth of the spot, they also significantly weaken the turbulence inside it.
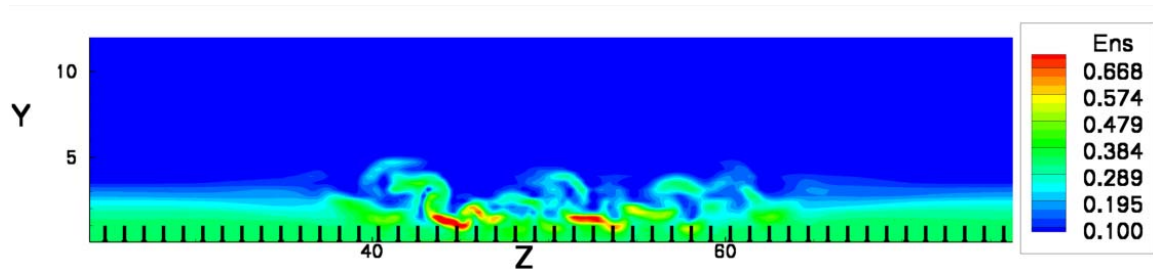


Figure 3.10: Contours of enstrophy on a zy plane located 212.8 $\delta_o^*$ downstream of the perturbation, at time t = 334.3 $\delta_o^*$/$U_\infty$ for a spot over h = 1.11 $\delta_o^*$ damping fins. The y and z axes have units of $\delta_o^*$, and the units of enstrophy (shown in the contour legend) are $U_\infty$/$\delta_o^*$.

**RIBLETS AND FINS**

The dramatic effect of damping fins on spot growth is impressive, but of course they are not physically realistic. The bulk of the work presented here was on riblets and fins, textures that could be applied in a practical engineering situation.

As discussed in Sect. 2, with damping fins the same relaxed laminar profile can be used for any combination of fin height and spacing, since the damping fins have no effect on the flow until it is perturbed. Riblets and real fins, however, significantly alter the laminar boundary layer profile in the region near the wall, and thus relaxation to a steady laminar state was performed with the textures already in the flow.

Figure 3.11 shows results for two cases with real fins and two cases with riblets, and the flat wall case is repeated for comparison. The domain, grid, and perturbation for the fin and riblet cases are the same as for the flat wall case, and the spot is shown at the same time intervals and with the same isosurface of |$\omega_x$| as in Fig. 3.1.
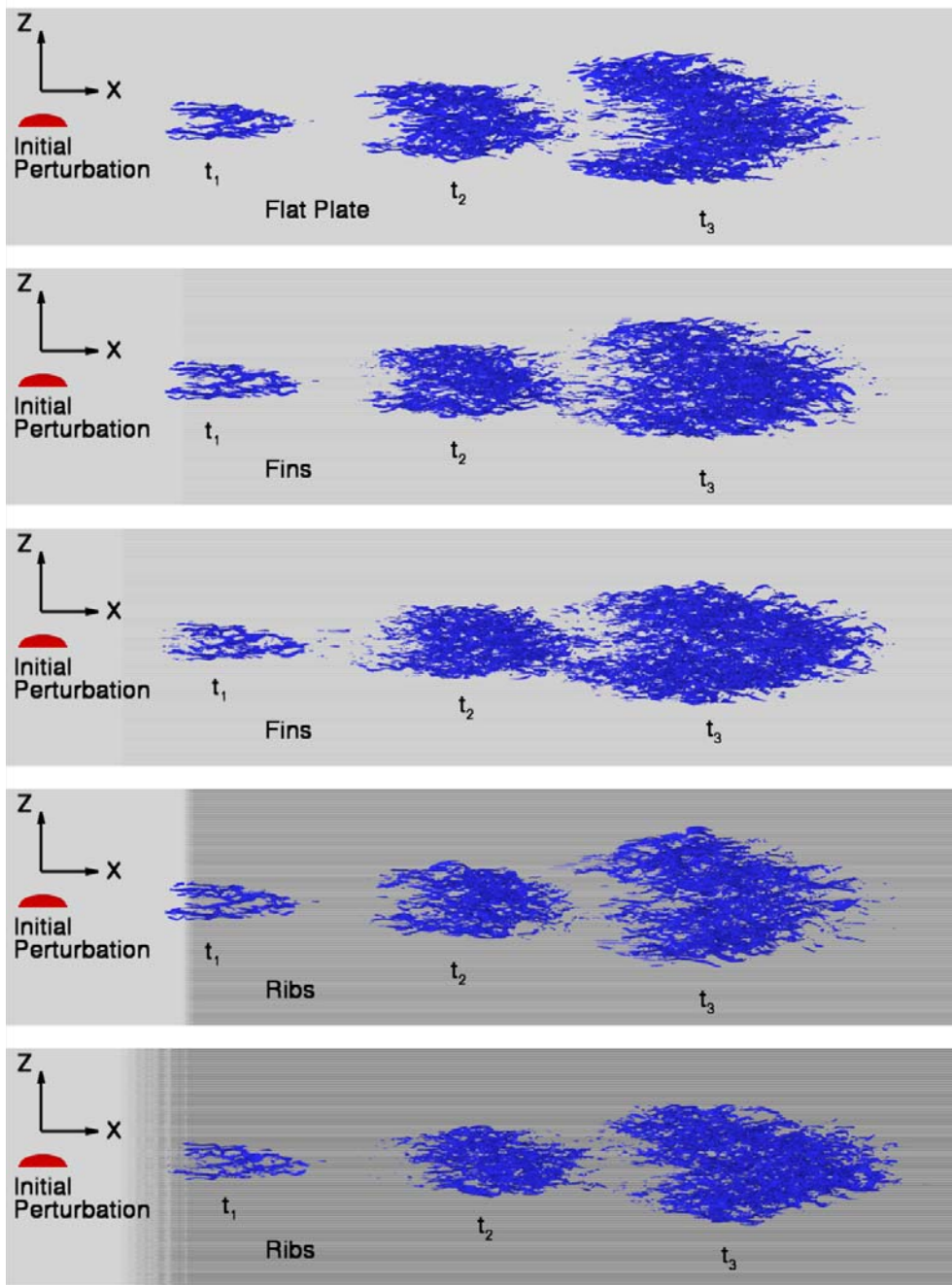
41

Figure 3.11: Top view of turbulent spots over a flat plate (top image), real fins (the next two images), and riblets (the last two images). Fin height was 0.53 $\delta_o^*$ and 0.80 $\delta_o^*$, for the top and bottom fin cases, respectively. Riblet height was 0.53 $\delta_o^*$ and 1.11 $\delta_o^*$ for the top and bottom riblet cases, respectively. In all four surface texture cases, the texture spacing was 1.11 $\delta_o^*$.

It is immediately apparent from the figure that unlike the damping fins, the real textures do not dramatically reduce spot growth. The spot shape changes from case to case, but with a chaotic process like turbulent spot growth it is not wise to read too much into changes in shape when comparing only a single run for each case, rather than an ensemble average. The overall arrowhead shape of the spot is maintained to a greater or lesser degree for all cases shown in the figure. The flat wall case is the most clearly arrowhead shaped, and the $h = 0.53 \, \delta_o^*$ fin case is the least. Though it is not dramatic, the lateral spread of the spot is somewhat decreased for both the $h = 0.80 \, \delta_o^*$ fin case and the $h = 0.80 \, \delta_o^*$ riblet case. Comparisons of lateral spread and spreading angle will be examined in great detail in Sect. 4. As with the spanwise damping fins, the front tip velocity of the spots is not altered significantly by the textures.

Figure 3.12 shows zoomed in views of the top of the spot, for the flat wall, $h = 0.53 \, \delta_o^*$ real fin, and $h = 0.53 \, \delta_o^*$ riblet cases. There is not a great deal of qualitative difference between the spots. All three have the same intertwined hairpin structures, and roughly the same density of vortical structures inside the spot (none of the cases has clearly weaker or stronger turbulence inside the spot compared to the others). As noted on the figure, the flat wall spot does have long, streamwise vortical structures near both of the rear wingtips that are not present in the riblet or fin cases.

### COMPARISON OF DAMPING FINS WITH REAL TEXTURES

Why is it that damping fins are so effective at slowing spot growth while real textures are much less so? The primary reason can be seen in Figure 3.13, which shows zy slices of spots over a flat plate, damping fins, real fins, and two sizes of riblets. In the image for the flat plate case, the red (high enstrophy) regions extend down all the way to the plate. In the damping fin case the red regions also extend down to the plate (although

43

the turbulence inside the spot is considerably weaker, so there is less red in general in the image). In the real fin case, however, the red regions do not extend down to the plate in the spaces between the fins. Instead the red regions are found well above the base of the fins (the nominal wall location). The same is true of the riblet case, although the high enstrophy regions do drop down slightly more into the riblet valleys. Finally, in the case with taller riblets the effect is even more pronouced. The red regions remain almost completely above the riblet crests, and only slow flow is present in the riblet valleys. In order for the textures to damp the turbulent spanwise velocity fluctuations, these fluctuations must be present in the region of the textures. The region of slow flow created by the real textures (due to the no-slip condition on the streamwise velocity) forces the turbulent vortical structures up and away from the nominal wall location, and thus the textures are not able to greatly affect the spot. The damping fins, however, do not create this region of slow flow, and thus the turbulent structures remain near the wall where the damping fins can directly affect them.
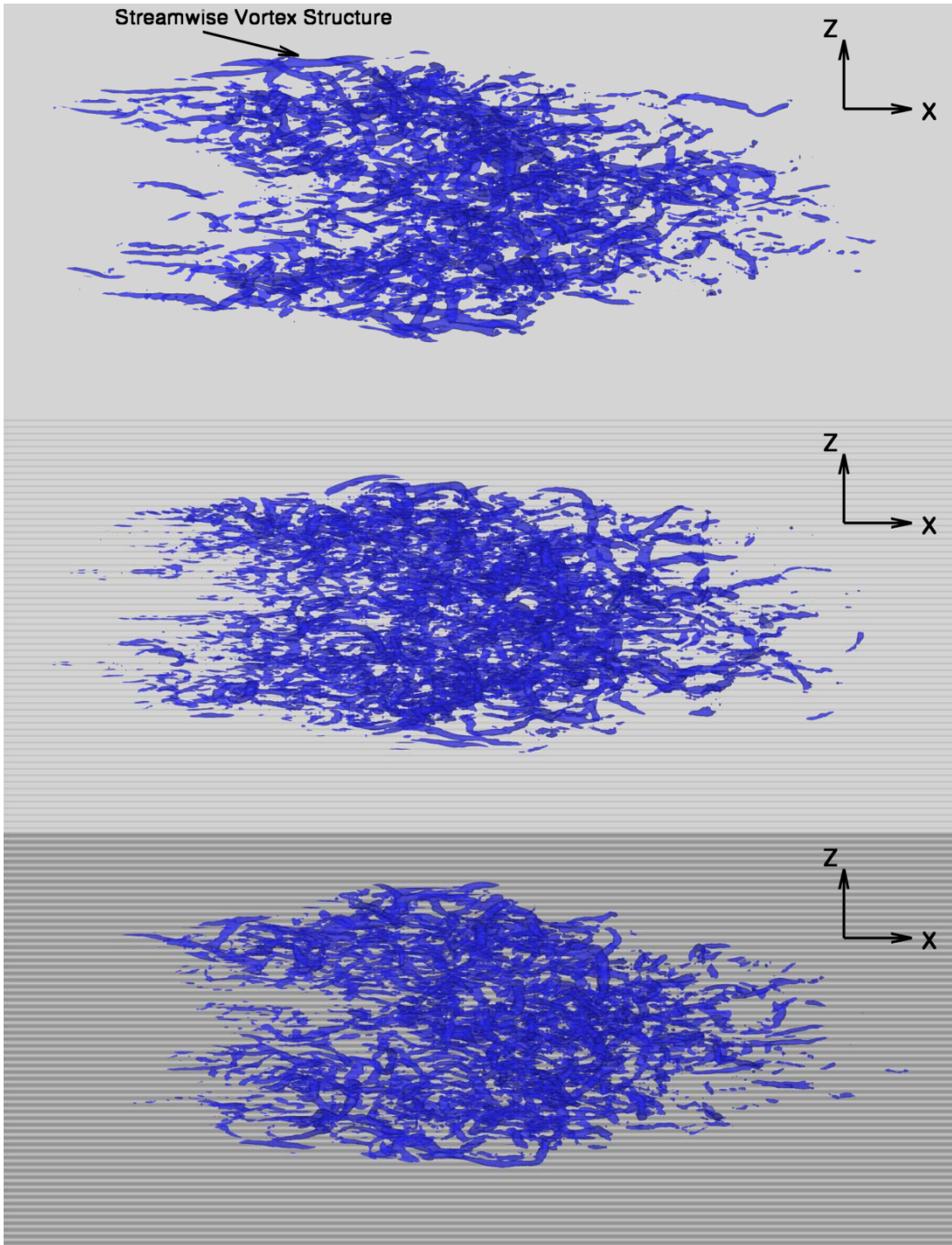
Figure 3.12: Closeup views of turbulent spots over a flat wall, h = 0.53 $\delta_o^*$ real fins, and h = 0.53 $\delta_o^*$ riblets (from top to bottom). Spots are drawn with an isosurface of $\lambda_2$ at the value of 0.0071 $(U_\infty/\delta_o^*)^2$, and shown at t = 398.0 $\delta_o^*/U_\infty$.
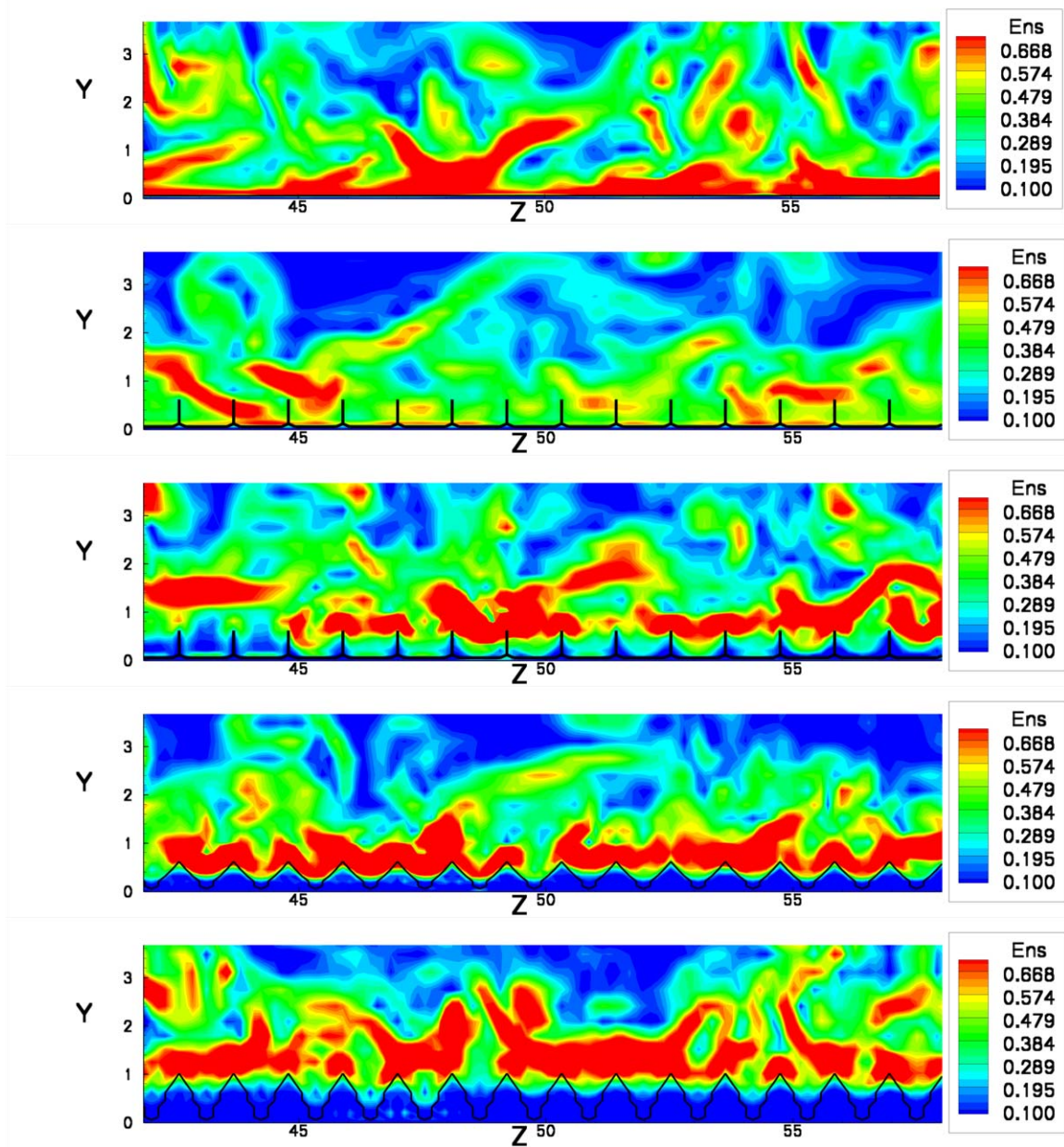
Figure 3.13: Contours of enstrophy on a zy plane located 212.8 $\delta_o^*$ downstream of the perturbation, at time t = 366.1 $\delta_o^*/U_\infty$. The y and z axes have units of $\delta_o^*$, and the units of enstrophy (shown in the contour legend) are $U_\infty/\delta_o^*$. From the top, the cases are flat plate, h = 0.532 $\delta_o^*$, s = 1.109 $\delta_o^*$ damping fins, h = 0.532 $\delta_o^*$, s = 1.109 $\delta_o^*$ real fins, h = 0.798 $\delta_o^*$, s = 1.109 $\delta_o^*$ riblets, and h = 1.064 $\delta_o^*$, s = 1.109 $\delta_o^*$ riblets.

# Chapter 4:  Quantitative Measures of Spot Growth and Spreading

**DEFINING THE SPOT**

As discussed previously, there are many ways to define the boundaries of a turbulent spot.  The majority of these involve a cutoff value for some specific flow variable.  If the value of the variable is greater than the cutoff value in a specific region, then that region is defined to be part of the spot, otherwise it is considered outside the spot.  Since one of the primary goals of this work is to investigate how the spreading of a spot is affected by surface textures, a consistent and precise definition of the spot is important.  Several factors influenced the decision on how to define the spot.  First, the chosen variables should have values near zero in a laminar, flat plate boundary layer.  Even when textures are introduced, in the laminar case the values of these variables should be small throughout the majority of the domain.  At the same time, their values should become quite large (relative to the laminar case) inside the spot, so that they are useful for picking out the spot from the background flow.  This is especially important in the surface texture cases, since many quantities that could normally be used to define the spot (such as enstrophy, vertical velocity, and the vertical compontent of vorticity) become large not only inside the spot, but also along the crests of the textures and in the region where the textures begin.  When examining so many different spots, at so many different time steps, it is impossible to accurately "eyeball" the output to determine the edge of the spot.  It is necessary to determine spreading angle in an automated way.  Thus, it is essential that the chosen quantities pick out the spot from the textures without the need for qualitative examination in every case.  The above considerations resulted in the choice of the swirling strength, $\lambda_2$, and the magnitude of the streamwise component of vorticity, $|\omega_x|$, as the variables which will define the spot.

The output from each run includes the 3D flowfield at a total of 40 different times (with an interval of 15.9 $\delta_o^*/U_\infty$ between each output time).  At each output time the location of the "right" and "left" lateral edges of the spot are determined.  Right and left are from the perspective of an observer looking downstream, from the trailing edge of the spot toward the front tip.  The right side of the spot is on the observer's right hand side, and the left side of the spot is on the observer's left hand side.  The spot edge (for either the right or left side) is defined as the point on the spot which is farthest from the spot centerline (a straight line which is drawn from the centroid of the perturbation, parallel to the freestream direction). The spot edge on each side is calculated with three different cutoff values of both $\lambda_2$ and $|\omega_x|$.  These six values are averaged to give one location for the spot edge on each side.  The cutoff vales for $\lambda_2$ are -0.00441 $(U_\infty/\delta_o^*)^2$, -0.00706 $(U_\infty/\delta_o^*)^2$, and -0.00883 $(U_\infty/\delta_o^*)^2$.  The cutoff values for $|\omega_x|$ are 0.188 $U_\infty/\delta_o^*$, 0.235 $U_\infty/\delta_o^*$, and 0.282 $U_\infty/\delta_o^*$.

Before averaging across the centerline, it must be shown that the spot spreading is not biased to the right or left side.  If the spot were to spread differently on one side (presumably due to the asymmetry of the initial perturbation), then it would be pointless to average the right and left hand sides to determine an overall spreading angle.  Instead, it would be necessary to report two different angles, one for each side.  Figure 4.1 shows how the distance from the centerline to the edge of the spot varies with streamwise location.  For this figure, the spot is defined by isosurfaces of $\lambda_2$ at the value of -0.00706 $(U_\infty/\delta_o^*)^2$ (which is one of the specific cutoff values listed above).  Both the left and right edges of the spot are shown.  It is clear that there is no bias in the spreading, since at some streamwise locations the spot has grown farther to the right, and at others it has grown farther to the left.  The right and left sides both follow a similar overall growth

pattern. Repeating this examination on multiple other spots led to the same conclusion, that the perturbation did not bias the spot growth in one direction or the other.
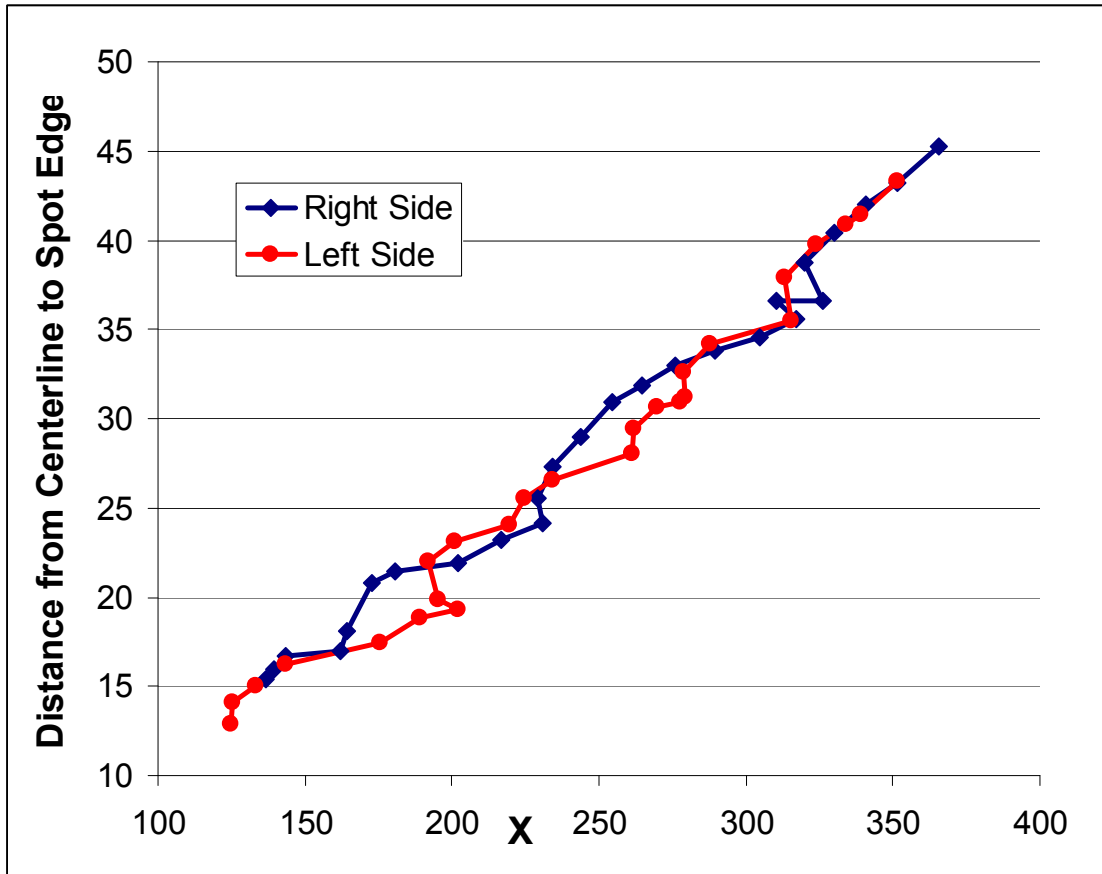


Figure 4.1: Distance from centerline to spot edge vs. streamwise location of the spot edge, for each side of an ensemble averaged spot over a flat plate. Spot is defined by isosurfaces of $\lambda_2$ at the value of -0.0071 $(U_\infty/\delta_o^*)^2$. Distances are in units of $\delta_o^*$.

Since the spot spreading is equivalent on the right and left sides, the two sides can be averaged to get one overall spot edge location at each output time interval. Once the spot has been averaged across the centerline, the spot edge location is equivalent to an average spot half-width. So, at every time interval, the final spot edge location is the

average of 12 values (the right edge location defined with 3 isosurfaces of $\lambda_2$ and with three isosurfaces of $|\omega_x|$, and the left edge defined with the same 6 isosurfaces). Note that average values are computed for both the distance from the spot centerline to the spot edge (the spot half-width), and for the streamwise location of the spot edge.

**DEFINING THE SPREADING ANGLE**

Even after defining the edges of the spot, it is still not completely clear what is meant by the "spreading angle". The key distinction is whether the spreading angle is measured from the perturbation, or from a virtual origin. Figure 4.2 illustrates the difference.
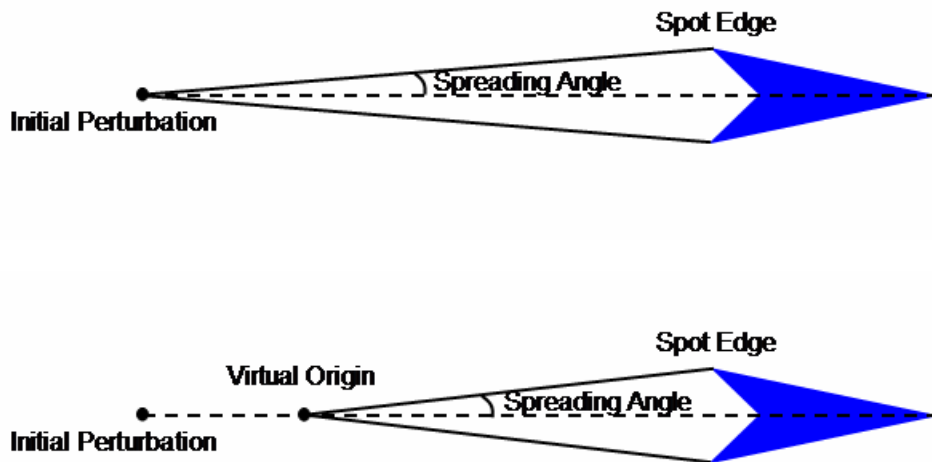


Figure 4.2: Spreading angle measured from the initial perturbation (top) and from a virtual origin downstream of the initial perturbation (bottom).

Several spots were examined to determine whether or not a virtual origin is appropriate. The ensemble averaged flat wall case is displayed in Figure 4.3. Two distinct growth regimes are present, indicating that a virtual origin should be used for the spreading angle. In the region just downstream of the perturbation, the very young spot

grows slowly, and the growth does not follow a linear pattern. This non-linear growth rate can be clearly seen in Figure 4.4, where the spot half-width is plotted against the streamwise location of the spot edge. Further downstream the growth rate takes on a reasonably constant value, and in this region a line can be fit through the spot edge locations, as is done in Figure 4.5. Note that these two figures overlap some (the data points between $x \approx 140\ \delta_o^*$ and $x \approx 200\ \delta_o^*$ are shown in both figures). Using linear regression to calculate the equation for this line, the spreading angle and the location of the virtual origin can easily be determined.
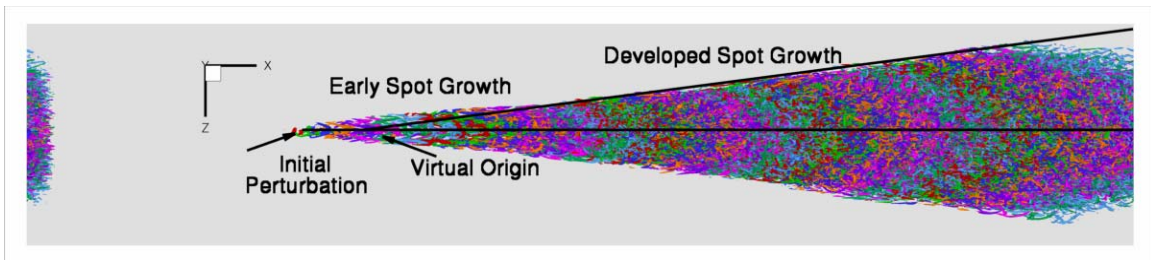


Figure 4.3:  Spot growth over a flat plate. Spot is shown with different colors at each output interval, and is defined by isosurfaces of $\lambda_2$ at the value of -0.0071 $(U_\infty/\delta_o^*)^2$.
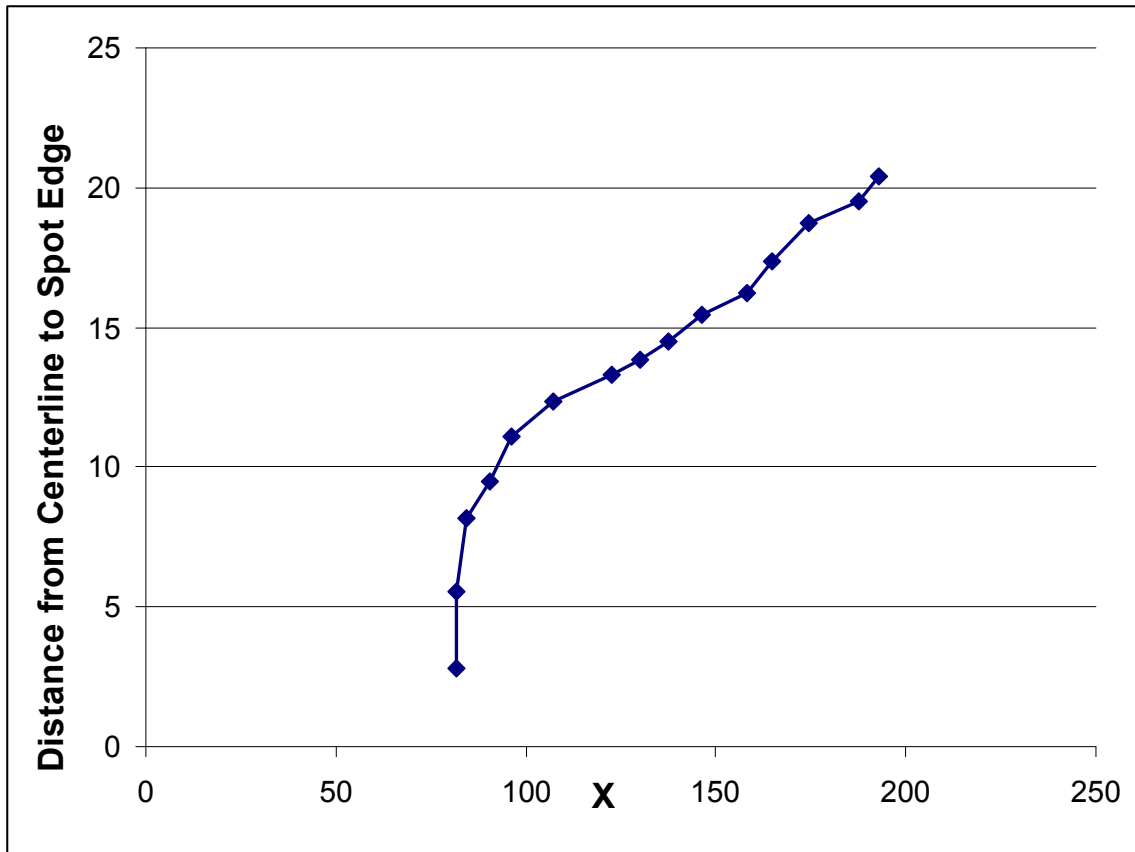
Figure 4.4:    Early spot growth over a flat plate.  Note the non-linear early growth of the pre-turbulent spot.  Both axes are in units of $\delta_o^*$.
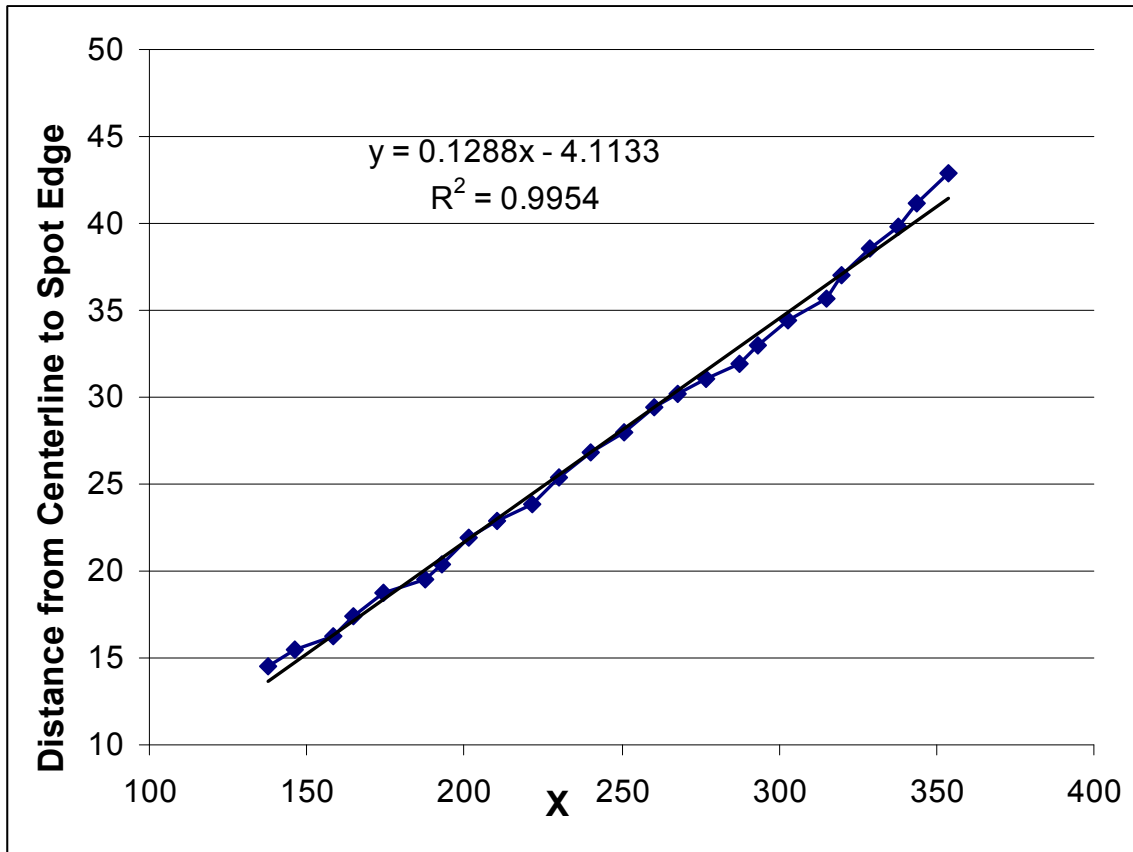
Figure 4.5:   Developed spot growth over a flat plate.  Note the linear growth of the spot, as indicated by the very high $R^2$ value for the linear trendline.  Both axes are in units of $\delta_o^*$.

## SPREADING ANGLE RESULTS

The method described above was used to calculate the spreading angle and virtual origin for the spots examined here, and the results are listed in Tables 4.1 and 4.2.

Table 4.1:  Spreading angles and virtual origins, calculated by the method described above, for spots over the flat wall and over riblets.  Note that the virtual origin is located downstream of the initial perturbation.  The riblet height is h, and the riblet crest-to-crest spacing is s.  Rows with average values are in bold.

| | Spreading Angle (°) | Virtual Origin (units of $\delta_o^*$) |
|---|---|---|
| Flat Wall - Spot1 | 7.15 | 31.8 |
| Flat Wall - Spot2 | 6.88 | 9.0 |
| Flat Wall - Spot3 | 6.97 | 26.7 |
| Flat Wall - Spot4 | 7.01 | 21.7 |
| **Flat Wall - Arithmetic Average** | **7.00** | **22.3** |
| **Flat Wall - Ensemble Average** | **7.34** | **31.8** |
| Flat Wall - No Suction Wall | 5.49 | 15.6 |
| Ribs, h = 0.532 $\delta_o^*$, s = 1.109 $\delta_o^*$ - Spot1 | 7.52 | 49.6 |
| Ribs, h = 0.532 $\delta_o^*$, s = 1.109 $\delta_o^*$ - Spot2 | 7.21 | 44.5 |
| Ribs, h = 0.532 $\delta_o^*$, s = 1.109 $\delta_o^*$ - Spot3 | 6.45 | 22.7 |
| Ribs, h = 0.532 $\delta_o^*$, s = 1.109 $\delta_o^*$ - Spot4 | 6.93 | 38.3 |
| **Ribs, h = 0.532 $\delta_o^*$, s = 1.109 $\delta_o^*$ - Arithmetic Average** | **7.03** | **38.8** |
| **Ribs, h = 0.532 $\delta_o^*$, s = 1.109 $\delta_o^*$ - Ensemble Average** | **7.16** | **42.0** |
| Ribs, h = 0.798 $\delta_o^*$, s = 1.109 $\delta_o^*$ - Spot1 | 6.72 | 52.7 |
| Ribs, h = 0.798 $\delta_o^*$, s = 1.109 $\delta_o^*$ - Spot2 | 6.31 | 23.5 |
| Ribs, h = 0.798 $\delta_o^*$, s = 1.109 $\delta_o^*$ - Spot3 | 6.84 | 51.7 |
| Ribs, h = 0.798 $\delta_o^*$, s = 1.109 $\delta_o^*$ - Spot4 | 7.46 | 46.6 |
| **Ribs, h = 0.798 $\delta_o^*$, s = 1.109 $\delta_o^*$ - Arithmetic Average** | **6.83** | **43.6** |
| **Ribs, h = 0.798 $\delta_o^*$, s = 1.109 $\delta_o^*$ - Ensemble Average** | **7.03** | **46.4** |
| Ribs, h = 0.798 $\delta_o^*$, s = 1.663 $\delta_o^*$ - Spot1 | 6.61 | 41.7 |
| Ribs, h = 0.798 $\delta_o^*$, s = 1.663 $\delta_o^*$ - Spot2 | 6.32 | 32.4 |
| Ribs, h = 0.798 $\delta_o^*$, s = 1.663 $\delta_o^*$ - Spot3 | 6.75 | 47.7 |
| Ribs, h = 0.798 $\delta_o^*$, s = 1.663 $\delta_o^*$ - Spot4 | 6.53 | 29.8 |
| **Ribs, h = 0.798 $\delta_o^*$, s = 1.663 $\delta_o^*$ - Arithmetic Average** | **6.55** | **37.9** |
| **Ribs, h = 0.798 $\delta_o^*$, s = 1.663 $\delta_o^*$ - Ensemble Average** | **6.66** | **41.5** |
| Ribs, h = 1.064 $\delta_o^*$, s = 1.109 $\delta_o^*$ - Spot1 | 6.79 | 59.6 |
| Ribs, h = 1.064 $\delta_o^*$, s = 1.109 $\delta_o^*$ - Spot2 | 6.01 | 27.5 |
| Ribs, h = 1.064 $\delta_o^*$, s = 1.109 $\delta_o^*$ - Spot3 | 6.33 | 42.0 |
| Ribs, h = 1.064 $\delta_o^*$, s = 1.109 $\delta_o^*$ - Spot4 | 6.61 | 27.3 |
| **Ribs, h = 1.064 $\delta_o^*$, s = 1.109 $\delta_o^*$ - Arithmetic Average** | **6.44** | **39.1** |
| **Ribs, h = 1.064 $\delta_o^*$, s = 1.109 $\delta_o^*$ - Ensemble Average** | **6.45** | **34.1** |

Table 4.2: Spreading angles and virtual origins, calculated by the method described above, for spots over fins and spanwise damping fins. Note that the virtual origin is located downstream of the initial perturbation. The runs with h = 1.064 $\delta_o^*$ fins had problems with Gibbs phenomena, and so a spreading angle and virtual origin could not be determined accurately (see Figure 4.8). A spreading angle also could not be calculated for the run with h = 1.064 $\delta_o^*$ damping fins because in this case the spot actually decreases in half-width as it moves over the damping fins. The fin height is h, and the fin spacing is s. Rows with average values are in bold.

| | Spreading Angle (°) | Virtual Origin (units of $\delta_o^*$) |
|---|---|---|
| Fins, h = 0.532 $\delta_o^*$, s = 1.109 $\delta_o^*$ - Spot1 | 6.00 | 19.0 |
| Fins, h = 0.532 $\delta_o^*$, s = 1.109 $\delta_o^*$ - Spot2 | 7.21 | 44.5 |
| Fins, h = 0.532 $\delta_o^*$, s = 1.109 $\delta_o^*$ - Spot3 | 6.45 | 22.7 |
| Fins, h = 0.532 $\delta_o^*$, s = 1.109 $\delta_o^*$ - Spot4 | 6.93 | 38.4 |
| **Fins, h = 0.532 $\delta_o^*$, s = 1.109 $\delta_o^*$ - Arithmetic Average** | **6.65** | **31.2** |
| **Fins, h = 0.532 $\delta_o^*$, s = 1.109 $\delta_o^*$ - Ensemble Average** | **6.68** | **36.7** |
| Fins, h = 0.798 $\delta_o^*$, s = 1.109 $\delta_o^*$ - Spot1 | 5.76 | 12.6 |
| Fins, h = 0.798 $\delta_o^*$, s = 1.109 $\delta_o^*$ - Spot2 | 6.11 | 20.7 |
| Fins, h = 0.798 $\delta_o^*$, s = 1.109 $\delta_o^*$ - Spot3 | 5.86 | 15.7 |
| Fins, h = 0.798 $\delta_o^*$, s = 1.109 $\delta_o^*$ - Spot4 | 5.97 | 14.9 |
| **Fins, h = 0.798 $\delta_o^*$, s = 1.109 $\delta_o^*$ - Arithmetic Average** | **5.93** | **16.0** |
| **Fins, h = 0.798 $\delta_o^*$, s = 1.109 $\delta_o^*$ - Ensemble Average** | **5.98** | **24.5** |
| Fins, h = 0.798 $\delta_o^*$, s = 1.663 $\delta_o^*$ - Spot1 | 6.51 | 16.6 |
| Fins, h = 0.798 $\delta_o^*$, s = 1.663 $\delta_o^*$ - Spot2 | 6.48 | 5.2 |
| Fins, h = 0.798 $\delta_o^*$, s = 1.663 $\delta_o^*$ - Spot3 | 7.10 | 22.4 |
| Fins, h = 0.798 $\delta_o^*$, s = 1.663 $\delta_o^*$ - Spot4 | 9.05 | 7.2 |
| **Fins, h = 0.798 $\delta_o^*$, s = 1.663 $\delta_o^*$ - Arithmetic Average** | **7.29** | **12.9** |
| **Fins, h = 0.798 $\delta_o^*$, s = 1.663 $\delta_o^*$ - Ensemble Average** | **10.83** | **78.5** |
| Fins, h = 1.064 $\delta_o^*$, s = 1.109 $\delta_o^*$ - Spot1 | NA | NA |
| Fins, h = 1.064 $\delta_o^*$, s = 1.109 $\delta_o^*$ - Spot2 | NA | NA |
| Spanwise Damping Fins, h = 0.532 $\delta_o^*$, s = 1.109 $\delta_o^*$ | 4.20 | 19.8 |
| Spanwise Damping Fins, h = 0.798 $\delta_o^*$, s = 1.109 $\delta_o^*$ | 2.99 | 47.9 |
| Spanwise Damping Fins, h = 1.064 $\delta_o^*$, s = 1.109 $\delta_o^*$ | NA | NA |

As explained in Sect. 2, ensemble averaging was performed for the flat wall case, all of the riblet cases, and all of the fin cases except for the h = 1.064 $\delta_o^*$, s = 1.109 $\delta_o^*$ fins.  In the latter case, two spots were run, and both times large Gibbs phenomena prevented a spreading angle from being calculated, as shown in Fig. 4.8.  For this reason, no further runs were performed with the h = 1.064 $\delta_o^*$, s = 1.109 $\delta_o^*$ fins.  Only one run was performed for each of the damping fin cases and for the flat wall case with the suction wall turned off.  In addition to the ensemble averaged results the table also contains the results for each individual spot for each case.  The four slightly different perturbation shapes used to generate the runs referred to as Spot 1, Spot 2, Spot 3, and Spot 4 were described in Sect. 2.  In the cases where only one run was performed, the perturbation shape used was the one corresponding to Spot 1.  In the ensemble averaged cases, two different "average" spreading angles are reported.  The first is simply the spreading angle of the ensemble averaged spot, calculated in the same way as the spreading angle for any single run.  The second is the arithmetic average of the angles determined for each individual run.

A number of things are apparent from Table 4.1 and Table 4.2.  First, there can be significant variations between spots developing over identical surface textures, depending on the exact details of the initial perturbation.  The flat wall case shows relatively little variation between different runs.  The variation is larger for most of the riblet and fin cases.

Second, the spreading angle obtained by ensemble averaging the spots and then calculating the spreading angle can be significantly different from the results obtained by calculating a spreading angle for each spot, and then arithmetically averaging those four angles.  Even though the trendline fit to the data in each case is linear, the least-squares regression method used to produce that trendline is a non-linear procedure, and it is the

56

slope of this trendline which determines the spreading angle. This non-linearity means that the trendline, and thus the spreading angle, can be very sensitive to outliers (data points for which the spot-half width jumps suddenly due to a vortical structure arising near the lateral edge of the spot).

The third thing to notice is that there are two ways in which textures can affect spot spreading. One way is by increasing or decreasing the spreading angle, and the other is by altering the location of the virtual origin.

Comparing the ensemble averaged runs to one another, the smallest riblets have negligible effect on the spreading angle, but they do move the virtual origin downstream slightly. The smallest fins decrease the spreading angle, although still not by a significant amount, only about 8% of the flat wall value. They also move the virtual origin very slightly downstream.

Some of the other textures have a larger effect. For example, the ensemble averaged $h = 0.798 \, \delta_o^*$, $s = 1.663 \, \delta_o^*$ riblet case shows a decrease of 9% in the spreading angle compared to the ensemble averaged flat wall case, and the virtual origin is also moved $9.7 \, \delta_o^*$ further downstream. Similarly, the $h = 1.064 \, \delta_o^*$, $s = 1.109 \, \delta_o^*$ riblets decrease the spreading angle by 12% and move the virtual origin $2.3 \, \delta_o^*$ further downstream than in the flat wall case.

The $h = 0.798 \, \delta_o^*$, $s = 1.109 \, \delta_o^*$ fins provided a spreading angle decrease of 19%, the largest of the textures examined (counting only the real textures, not the spanwise damping fins). However, this fin configuration did move the virtual origin somewhat upstream of its flat wall location.

Finally, the spanwise damping fins were very effective at slowing spot spread. The small damping fins ($h = 0.798 \, \delta_o^*$, $s = 1.109 \, \delta_o^*$) decreased the spreading angle by 43% from the flat wall value, although they did move the virtual origin slightly upstream.

The midsize damping fins (h = 0.798 $\delta_o{}^*$, s = 1.109 $\delta_o{}^*$) decreased the spreading angle by 59% and also moved the virtual origin downstream. No spreading angle or virtual origin could be calculated for the largest damping fins (h = 1.064 $\delta_o{}^*$, s = 1.109 $\delta_o{}^*$), because they actually cause the spot half-width to *decrease* when the spot first moves over them. As it moves further downstream it begins to grow again slightly, but by the end of the run it is still smaller than it was when it first moved over the damping fins. It is clear from Fig. 4.9 that the large damping fins have all but completely stopped the spot from spreading.

Figures 4.6, 4.7, 4.8, and 4.9 give a visual idea of the spreading angles and virtual origins for several of the runs listed in Table 4.1. The images show the spot with isosurfaces of $\lambda_2$ at the value of -0.0071 $(U_\infty/\delta_o{}^*)^2$. All the single runs shown are for the first perturbation (i.e. Spot 1 is shown for each case). The virtual origin is shown in the correct location for each image, and the two diagonal lines represent the spreading angle calculated for that run. Note that each spot is shown with only one isosurface, and the lines do not exactly represent what the spreading angle would be if it were calculated with *that particular isosurface* (as opposed to being calculated from an average spot edge location based on six isosurfaces, as described above). Furthermore, the lines on both the left and right sides of the spot are based on the final spreading angle listed in Table 4.1, so they are symmetric about the spot centerline, even though at any given time the spot is not perfectly symmetric (as seen in Fig. 4.1).

As a test, a spot was allowed to develop over a flat wall with the suction wall turned off. With the suction wall off, a favorable pressure gradient exists in the streamwise direction, as discussed in Chapter 2. Katz et al. (1995) found that a strong favorable pressure gradient dramatically reduces spot growth. The pressure gradient in this case is not as strong as that used by Katz et al., but as seen from Table 2.1, the

58

spreading angle is nonetheless reduced by 25% compared to the ensemble averaged flat wall value.

This test was performed because in all of the simulations presented in this report a favorable pressure gradient develops in the channel, even with the suction wall left on. This occurs for two reasons. In all of the cases, once the spot begins to grow $d\delta^*/dx$ increases in the region in and around the spot, and thus more fluid is pushed up toward the suction wall. The suction wall is based on the analytical solution for a Blasius profile, and so far no way has been found to properly accommodate the extra fluid which is displaced upwards by the growing spot. Thus, a slight favorable pressure gradient develops, for the same reason that a favorable pressure gradient develops if the suction wall is turned off (see Chapter 2). In the cases with surface textures, $d\delta^*/dx$ appears greater than for the flat wall case even without the influence of the spot, and thus the vertical velocity far from the surface is increased. Again, the suction wall does not accommodate this extra vertical velocity, since it is based on the Blasius solution for a flat plate. No analytical solutions exist for boundary layer flow over textured surfaces, and it has proven very difficult to adjust the suction wall to maintain a true zero pressure gradient over the textures.

The pressure gradients created by the growing spot and by the textures are not as large as that created by removing the suction wall completely, and therefore should influence spot growth less. However, the influence of these pressure gradients on the growth of the spots will require further examination.
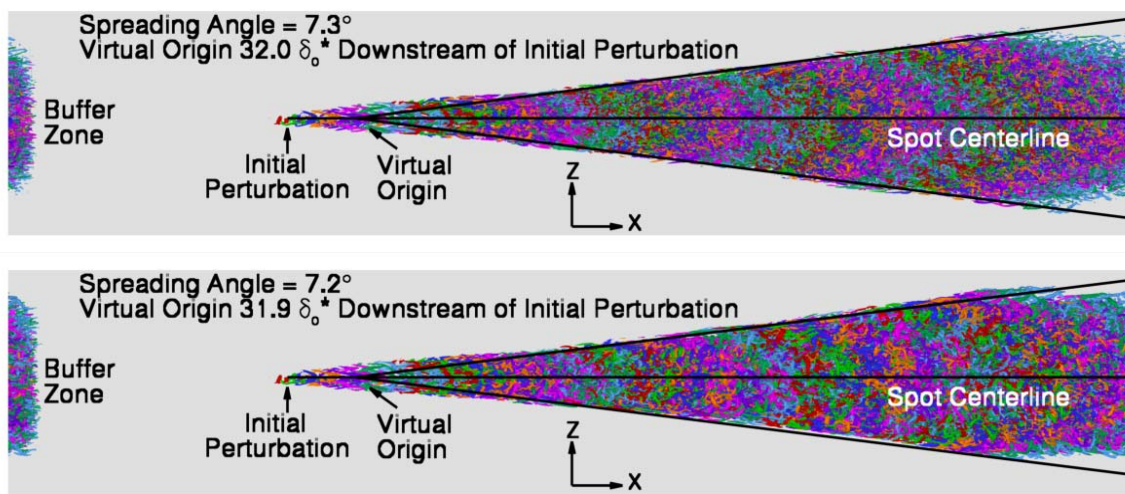
Figure 4.6: Top view of spot growth over a flat plate, drawn with isosurfaces of $\lambda_2$ at the value of -0.0071 $(U_\infty/\delta_o^*)^2$. Isosurfaces shown for multiple time steps simultaneously, in order to illustrate spot spreading angle. Top image is the ensemble averaged spot, bottom image is a single run.
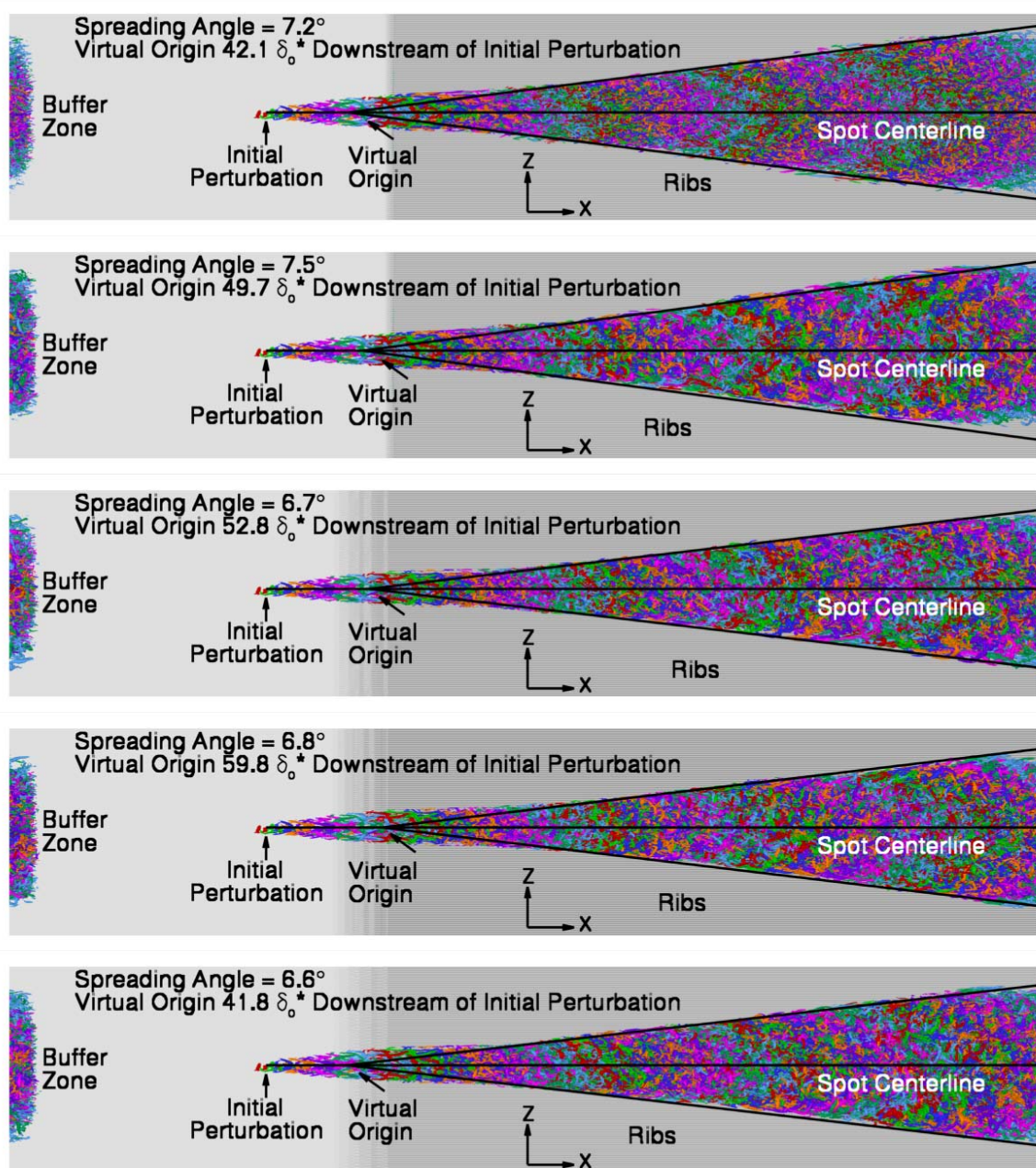
Figure 4.7: Top view of spot growth over riblets, drawn with isosurfaces of $\lambda_2$ at the value of -0.0071 $(U_\infty/\delta_o{}^*)^2$. From the top, the images are of the ensemble averaged case with h = 0.532 $\delta_o{}^*$, s = 1.109 $\delta_o{}^*$ riblets, a single run with those same riblets, and single runs of h = 0.798 $\delta_o{}^*$, s = 1.109 $\delta_o{}^*$ riblets, h = 1.064 $\delta_o{}^*$, s = 1.109 $\delta_o{}^*$ riblets, and h = 0.798 $\delta_o{}^*$, s = 1.663 $\delta_o{}^*$ riblets.
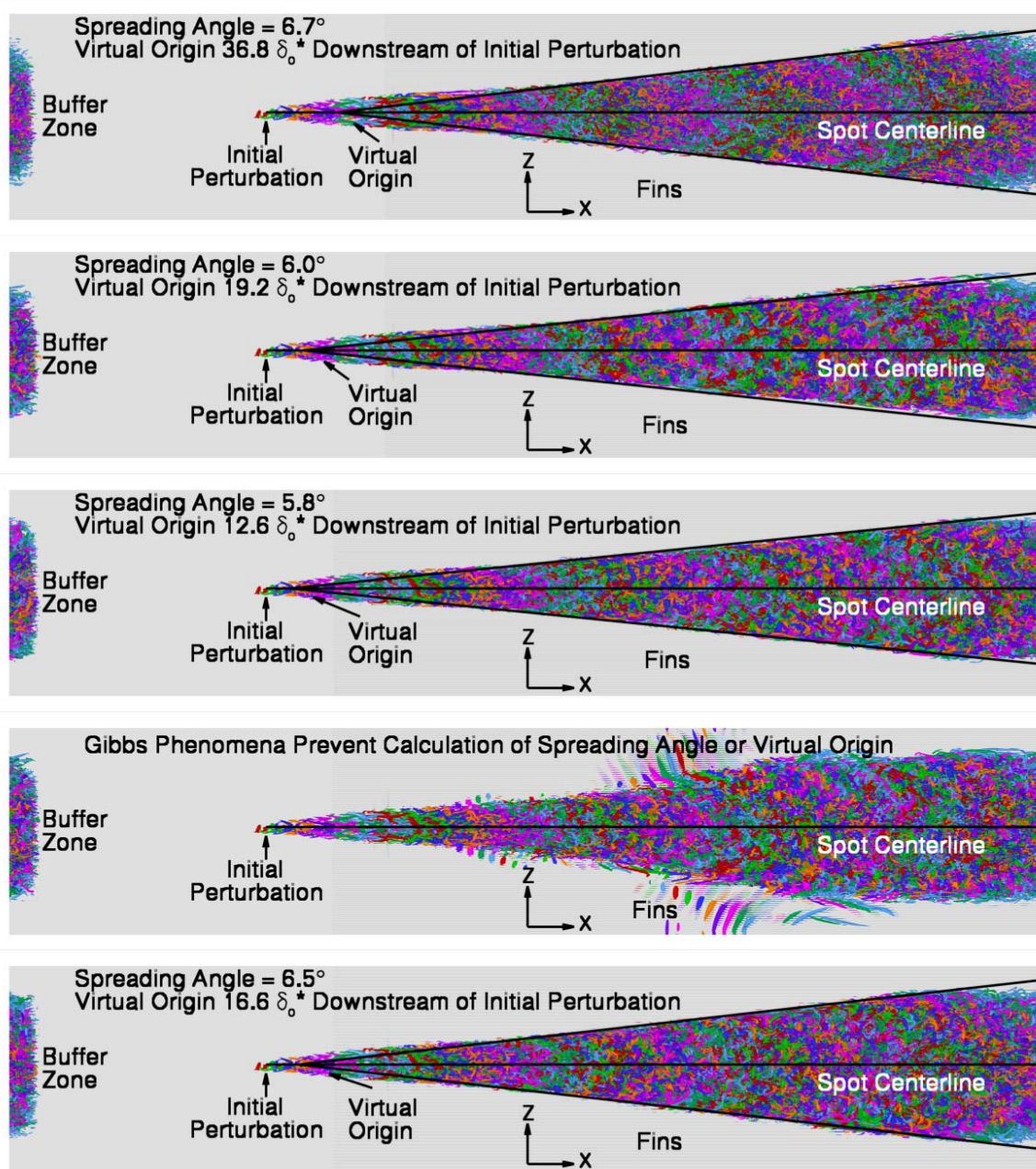
61

Figure 4.8: Top view of spot growth over real fins, drawn with isosurfaces of $\lambda_2$ at the value of -0.0071 $(U_\infty/\delta_o^*)^2$. From the top, the images are of the ensemble averaged case with $h = 0.532\ \delta_o^*$, $s = 1.109\ \delta_o^*$ fins, a single run with those same fins, and single runs of $h = 0.798\ \delta_o^*$, $s = 1.109\ \delta_o^*$ fins, $h = 1.064\ \delta_o^*$, $s = 1.109\ \delta_o^*$ fins, and $h = 0.798\ \delta_o^*$, $s = 1.663\ \delta_o^*$ fins.
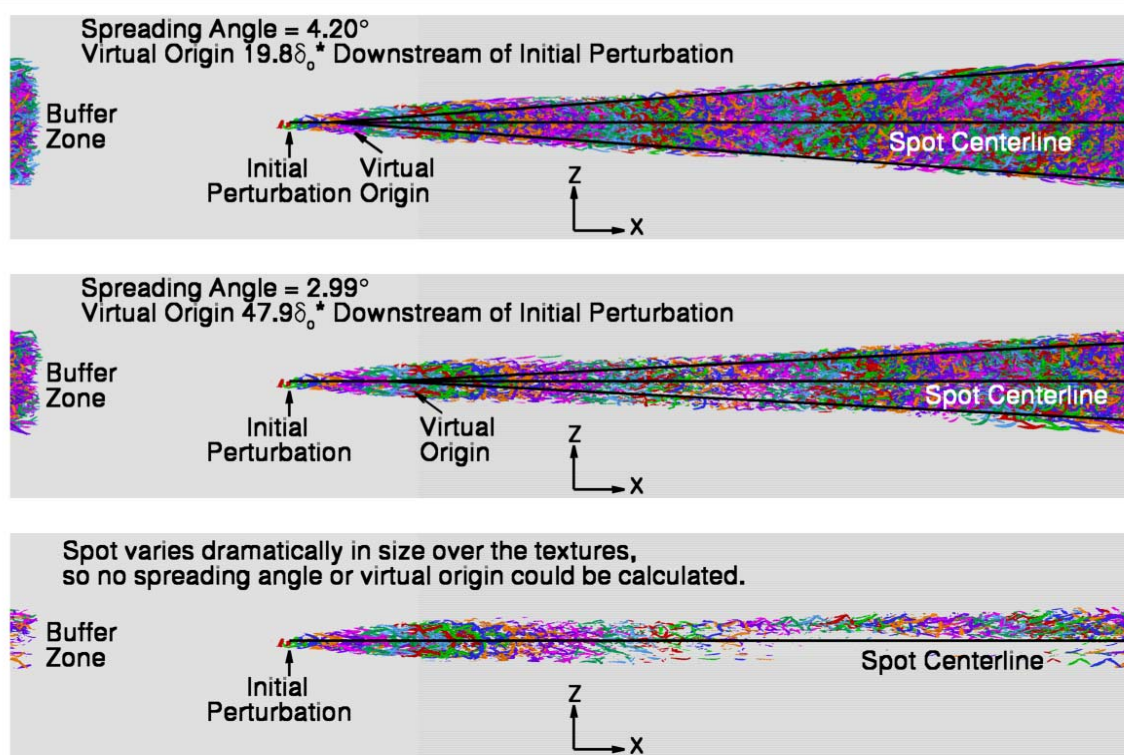
Figure 4.9:   Top view of spot growth over damping fins, drawn with isosurfaces of $\lambda_2$ at the value of $-0.0071 \ (U_\infty/\delta_o^*)^2$.  Damping fin heights are $0.532 \ \delta_o^*$, $0.798 \ \delta_o^*$, and $1.064 \ \delta_o^*$ in the top, middle, and bottom images, respectively.  In all three cases, damping fin crest-to-crest spacing is $1.109 \ \delta_o^*$.

# Chapter 5: Particles

In order to further elucidate the growth mechanisms of turbulent spots, the code was modified to allow individual fluid particles to be tracked as they move with the time-varying flowfield. Particles may be placed anywhere in the domain, and the number of particles is limited only by acceptable computation time. The position and velocity vectors of each particle are updated at every time step. The particle positions are not required to correspond to collocation points. Hermitian polynomials are used to calculate the velocity components of each particle. This interpolation method allows for velocity data for the entire flowfield to be taken into account when determining the velocity of a particle, and is thus significantly more accurate than linear interpolation. It is also somewhat computationally expensive, and thus in practice the number of particles must be limited to a few hundred, at most. A simple forward Euler scheme is used to move the particles at each time step.

It is important to note that although the particle motion is determined by the flowfield, the particles have absolutely no impact on the flow. In essence, the particles are a method of examining the results, similar to streamtraces, isosurfaces of specific variables, etc. which are calculated by postprocessing. Particle motion is only calculated in the code, while it is running, because storing the full 3D velocity field at every time step for posprocessing is impossible due to disk space constraints and network data transfer rates.

## VERIFICATION

It was necessary to verify that the velocity interpolation procedure was working properly, and that the time integration was sufficiently accurate. As discussed

previously, it is not feasible to simply output the 3D flowfield at every time step and use software (such as Tecplot) to calculate particle paths for comparison purposes. Instead, three cases were used to verify the accuracy of the particle motion. In the first case, a fluid which is initially at rest in a channel with shear free walls is accelerated by a uniform body force. The position of a particle determined by the code is compared to the analytical solution (which is simply a quadratic). Figure 5.1 displays the results of this case.
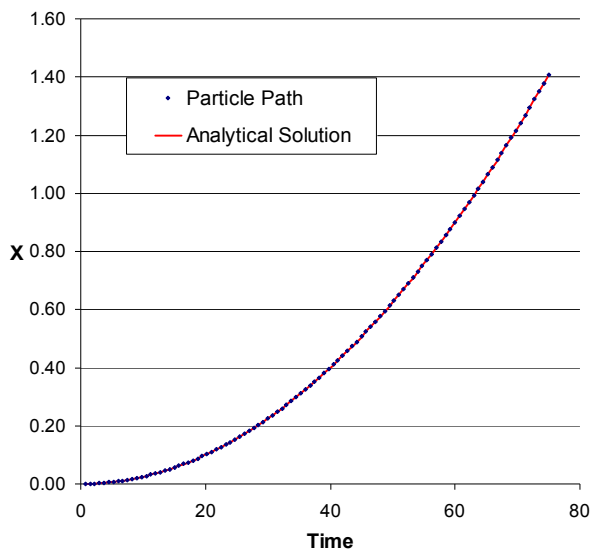


Figure 5.1:   Plot of particle position vs. time, symbols represent the particle position as calculated in the code, red line represents analytical solution.

For the second test, the path of a particle in a steady laminar boundary layer over riblets was compared with a streamline passing through the initial particle location. The streamline was calculated from the flowfield at one instant in time (using Tecplot), while the particle positions were calculated in the code as described above, and represent the motion of the particle over time. Since the flowfield is steady the particle path and

streamline should agree, as shown in Fig. 5.2. Note that Fig. 5.2 is stretched in the wall-normal direction for clarity.
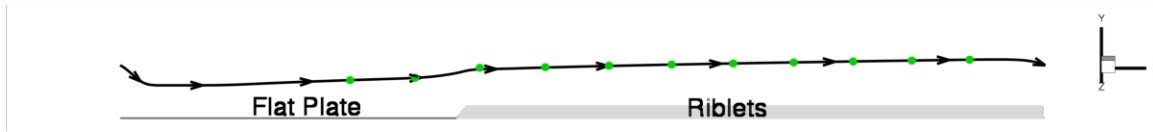


Figure 5.2: Particle positions (green dots) over time compared to a streamline passing through the initial particle location.

Finally, the particle motion method was tested with the flowfield in and around a turbulent spot. This case was used to test the time integration scheme for the particle motion. The particle motion subroutine was provided with the full 3D flowfield, and modified slightly so that this flowfield was treated as steady. Then, the particle paths were compared with instantaneous flowfield streamlines generated by Tecplot. Tecplot uses a 2$^{nd}$ order Runge-Kutta method for its time integration, while the particle motion subroutine uses simple forward Euler, but as seen in Figure 5.3, no difference can be detected, even when the streamline passes through the heart of the turbulent spot.
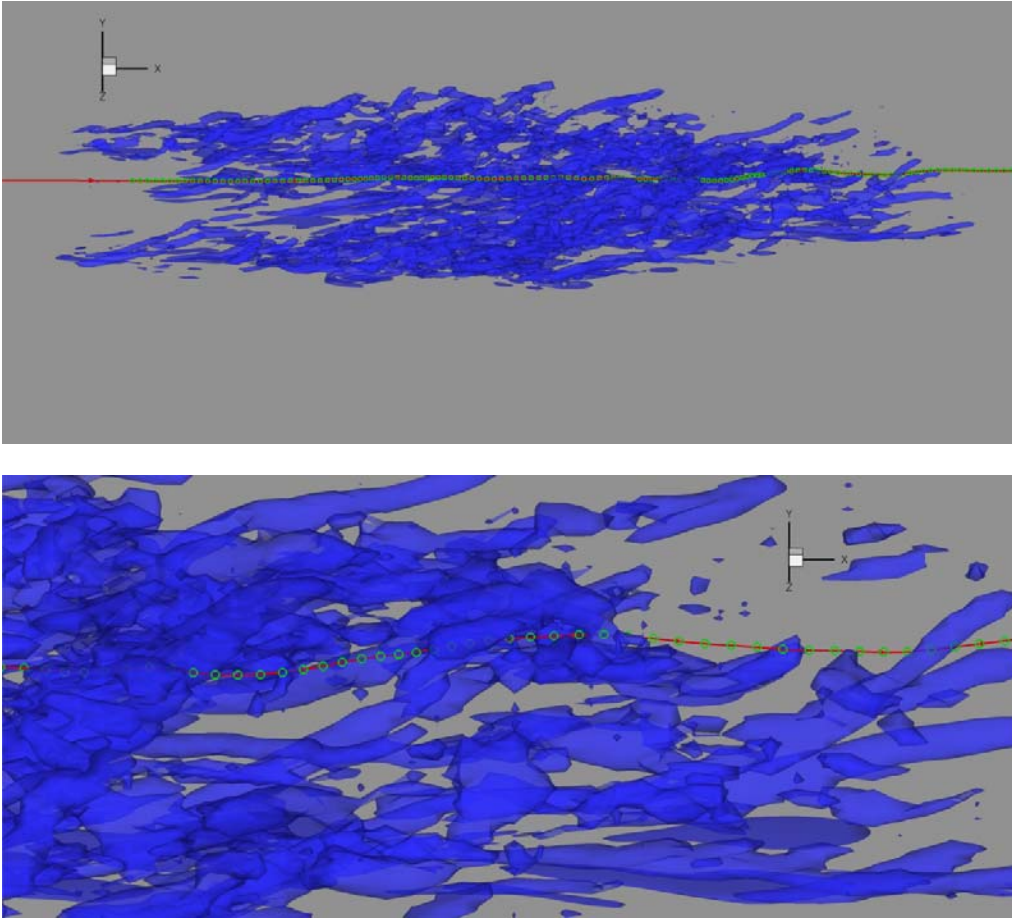
Figure 5.3: Particle path (the green circles) through an instantaneous flowfield which is treated as steady, compared to an instantaneous streamline (the red line) passing through the initial particle location. Top image shows overall spot, bottom image is zoomed in to display the extremely close agreement between the particle path and the streamline.

### INITIAL PARTICLE SEEDING

Particle motion was examined for three different spots: one over a flat plate, one over riblets with height and spacing of 0.532 $\delta_o^*$ and 1.109 $\delta_o^*$, respectively, and one over fins with the same height and spacing. In all three cases, the particles were "seeded" into the flow at a time 1596.5 $\delta_o^*/U_\infty$ after the initiation of the perturbation. Particles are initially placed on collocation points where $|\omega_x| \geq 0.282 \ U_\infty/\delta_o^*$. Due to computational time limits, only one particle is placed for every hundred collocation points which meet

the criteria above.  The particles are still distributed throughtout the spot, there are simply fewer of them than there would be if a particle was placed on every collocation point which met the criteria.  In all cases, the particles were tracked for a time of 3193.0 $\delta_o^*/U_\infty$.  The initial particle locations relative to the spot for each case (flat wall, riblets, and fins) can be seen in Figure 5.4.  It is clear that even though they are distributed somewhat sparcely, the particles nonetheless capture the overall size and shape of the spot at this early stage.  At the time the seeding occurred, the leading edge of the spot was about 110 $\delta_o^*$ downstream of the perturbation.

### PARTICLE MOTION

With all the preliminary steps sorted out, it is now possible to observe particles as they move downstream.  Figure 5.5 shows the spot and the particles at all output time steps on the same image for the flat wall, the fins, and the riblets.  The purpose of these images is to demonstrate that the spot spreads more rapidly than the particles in the spanwise direction, while at the same time some of the particles convect downstream faster than the spot.  This is clearly true in all three cases, since the green isosurface which represents the spot extends farther from the centerline than the blue dots which represent the particles, while the blue dots extend further than the green isosurface in the streamwise direction.  The same isosurface is used to identify the spot as was used to seed the particles in the first place ($|\omega_x| = 0.282\ U_\infty/\delta_o^*$).

Figure 5.6 shows the spot and particles at the last output time step for these runs, at a time 3193.0 $\delta_o^*/U_\infty$ after the particles are initially seeded into the flow.  Again all three cases (flat wall, riblets, and fins) are present.  Several intersting things can be seen here.  First, as mentioned above, many of the particles leave the spot entirely.  Some of the particles are left behind as the spot convects downstream, and others move out ahead

68

of the spot.  The reason why these particles leave the spot can be better seen in Fig. 5.7, which shows side views of the three spots taken at the same instant in time as the images in Fig. 5.6.  The particles that are left behind the spot are all located very near the wall, in the region where the streamwise velocity of the background laminar boundary layer is very low.  Thus, since the trailing edge of the spot moves at a velocity greater than 0.5 $U_\infty$, these particles are quickly left in the wake of the spot.  On the other hand, the particles that move out in front of the spot are located near or above the top of the spot, and are in a region where the streamwise velocity of the background laminar boundary layer approaches $U_\infty$.  Thus, since the front tip of the spot moves at $\sim$0.9 $U_\infty$, these particles move downstream faster than the spot.

It appears from these results that the spread of the spot is not the result of turbulent diffusion, since fluid particles that were once part of the spot (i.e. were located in regions of high streamwise vorticity) can later be found in regions of laminar flow.  If the spot were spreading because of diffusion, it would be expected that regions of the flowfield reached by particles that were once part of the spot would themselves be turbulent.  This is clearly not the case, since the spot spreads faster than the particles in the spanwise direction, and more slowly than the particles in the streamwise and wall-normal directions.  Instead, it appears that the spot must spread by a different process, most likely by driving the growth of instabilities in the surrounding laminar boundary layer, as proposed by Gad-El-Hak et al. (1981).
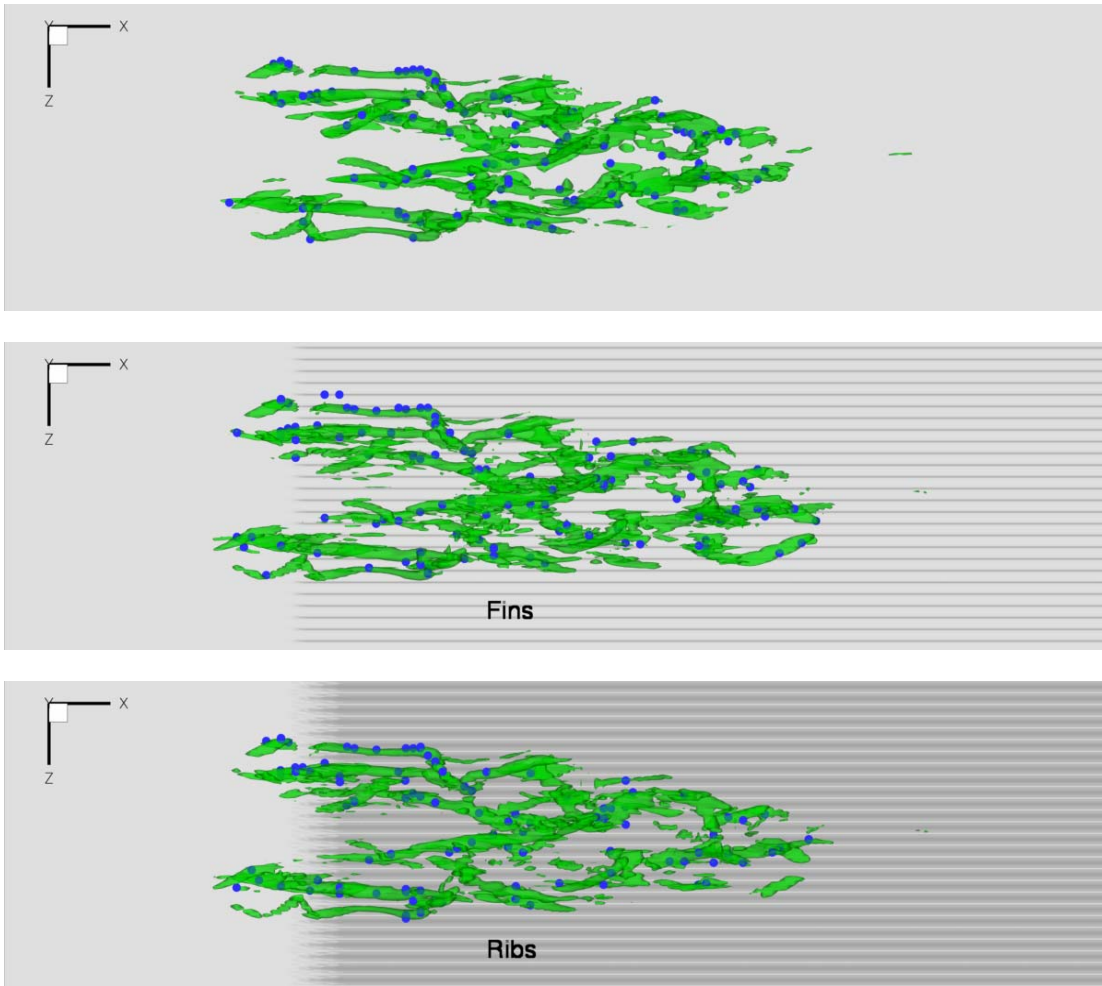
Figure 5.4: Top view of the initial distribution of particles for the flat plate (top), fin (middle), and riblet (bottom) cases. Each blue dot represents one particle. The spot is displayed with isosurfaces of $|\omega_x|$ at the value of $0.282\ U_\infty/\delta_o^*$.
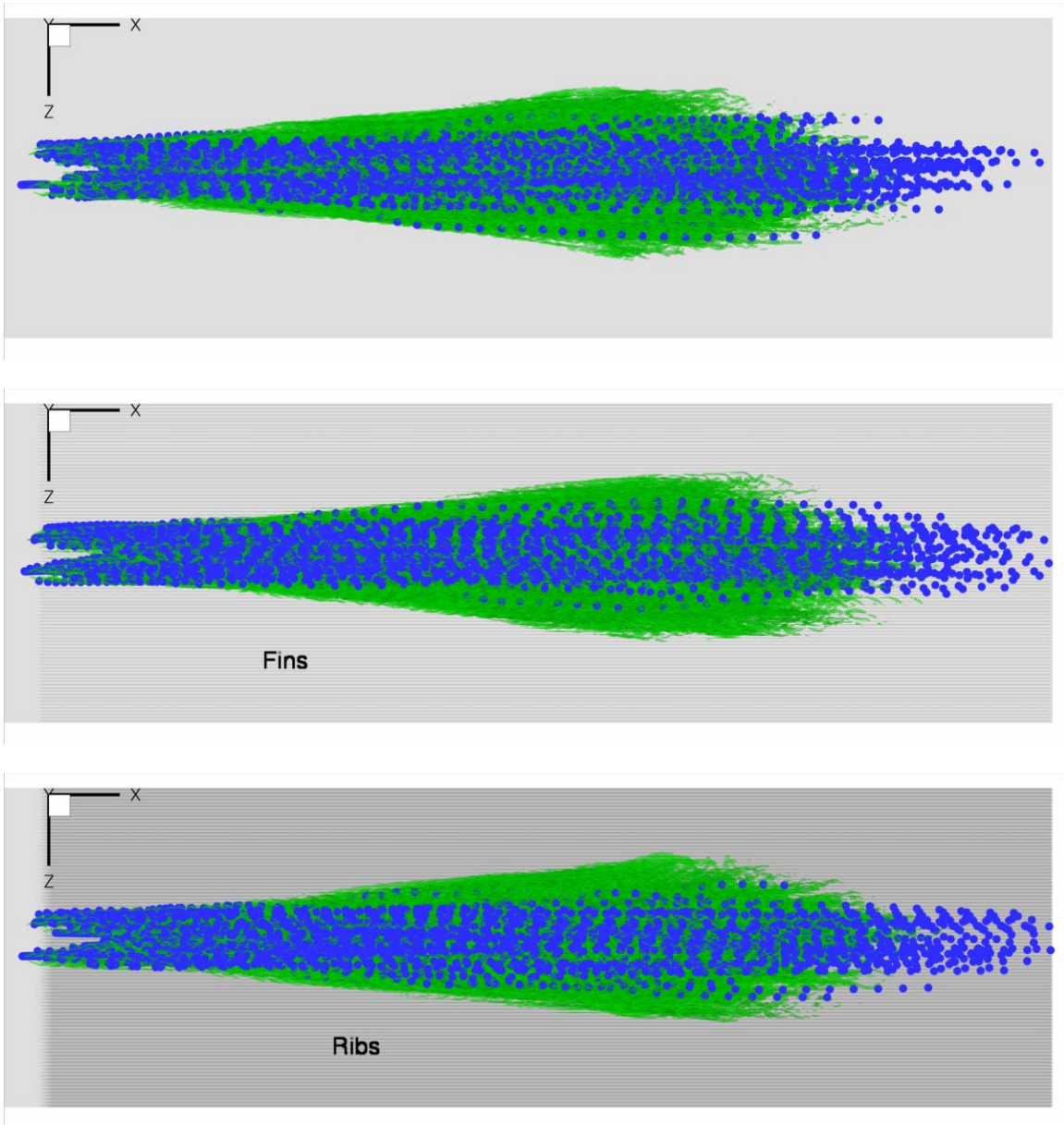
Figure 5.5: Spreading of spots vs. spreading of particles. The spot is shown in green, again with an isosurface of $|\omega_x|$ at the value of $0.282\, U_\infty/\delta_o^*$. Output at all time intervals are shown in the same color, and all the particles at each step also have the same symbol and color.
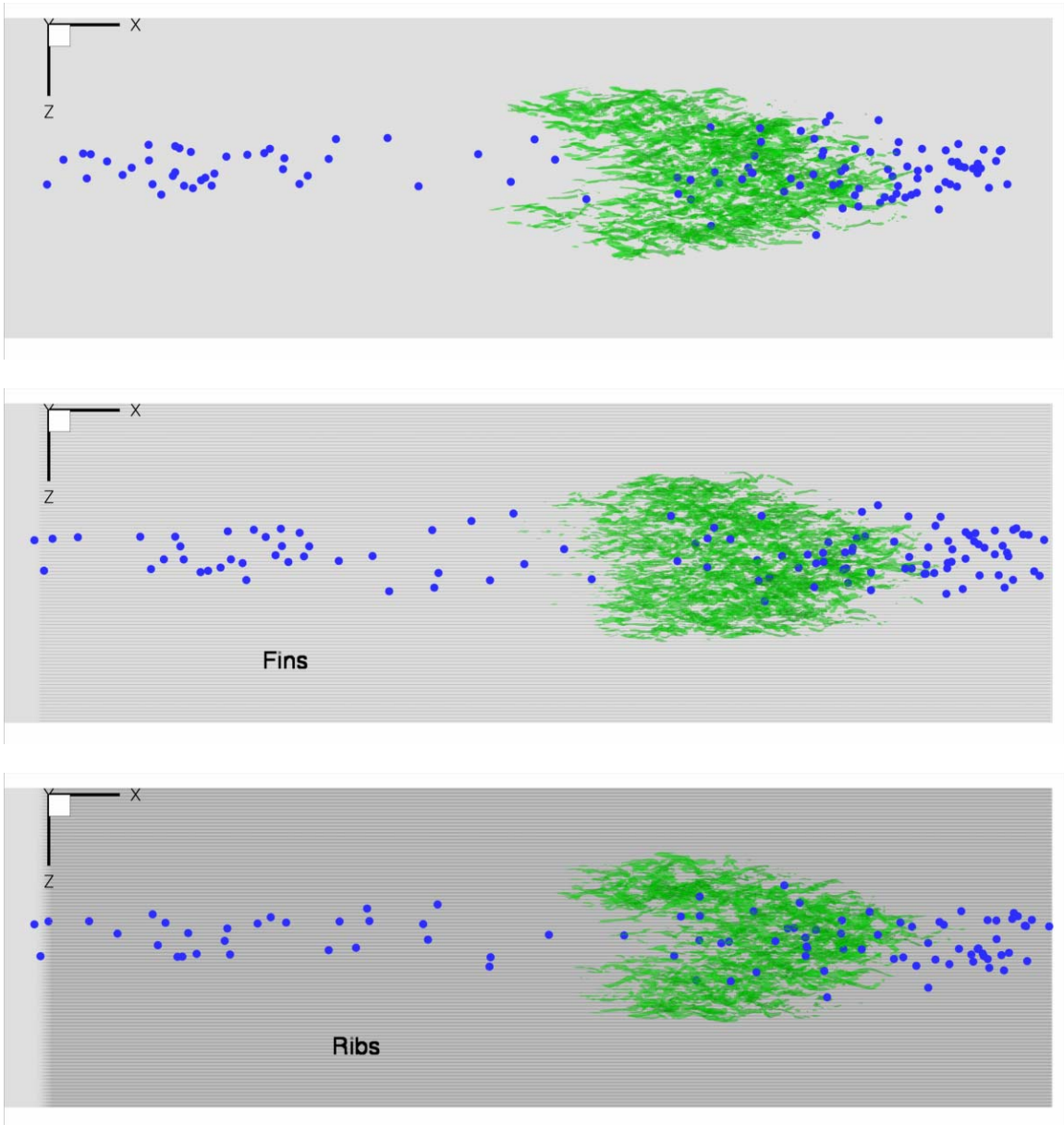
Figure 5.6: Top view of the distribution of particles for the flat plate (top), fin (middle), and riblet (bottom) cases after a time of 3193.0 $\delta_o^*/U_\infty$ from when the particles were seeded into the flow. Each blue dot represents one particle. The spot is displayed with isosurfaces of $|\omega_x|$ at the value of 0.282 $U_\infty/\delta_o^*$.
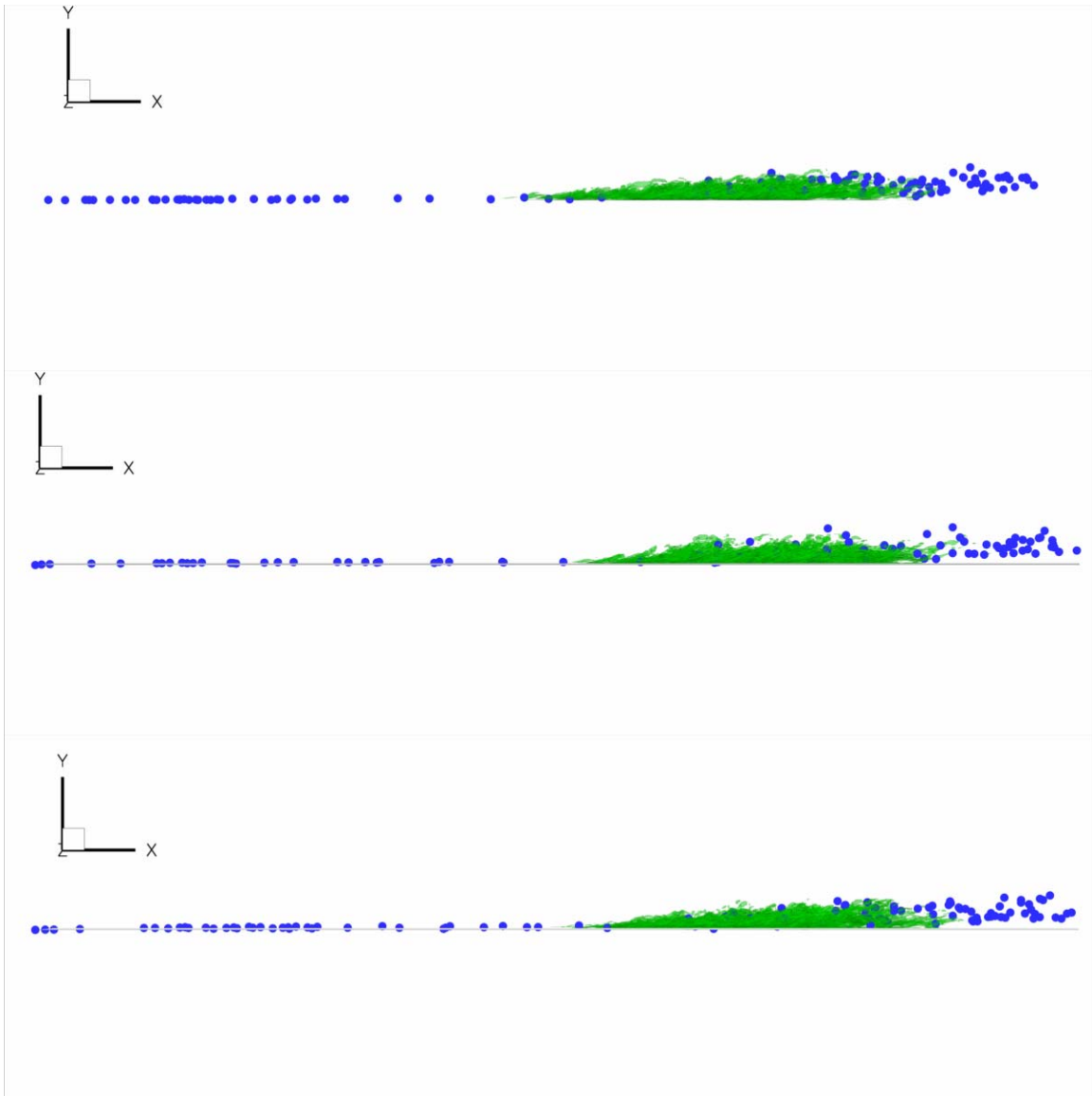
Figure 5.7: Side view of the distribution of particles for the flat plate (top), fin (middle), and riblet (bottom) cases after a time of 3193.0 $\delta_o^*/U_\infty$ from when the particles were seeded into the flow. Each blue dot represents one particle. The spot is displayed with isosurfaces of $|\omega_x|$ at the value of 0.282 $U_\infty/\delta_o^*$

.

# Chapter 6: Conclusions

Several conclusions can be drawn from the work presented here. First of all, it is possible with the suction wall method to simulate a boundary layer spot with a CFD code originally designed for channel flow. It is also possible to use the immersed boundary method to simulate spot growth over a flat plate and over various textured surfaces.

Concerning the goal of constraining spot growth, the spanwise damping fin cases demonstrate that if the spanwise velocity fluctuations in the near-wall region can be strongly damped, spot growth and spreading can be greatly decreased. What is not clear is whether any real texture is capable of damping these fluctuations in a developing spot strongly enough to significantly constrain spot growth. In the case of the smallest riblets, the spreading angle is not greatly effected. The ensemble averaged spreading angle is 2.5% lower than the flat wall value, but the arithmetic average of the spreading angles for the four runs is actually slightly higher than the arithmetic average for the four flat wall runs. The smallest fins had a slightly more noticable effect; they decreased the ensemble averaged spreading angle by 9% and the arithmetically averaged spreading angle by 5%.

Several of the larger textures had more significant effects. The best case for the fins ($h = 0.798 \, \delta_o^*$, $s = 1.109 \, \delta_o^*$) decreased the spreading angle by 19% of the flat wall value, and the best case for the riblets ($h = 1.064 \, \delta_o^*$, $s = 1.663 \, \delta_o^*$) decreased the spreading angle by 12%. If these decreases in spreading angle remain after accounting for pressure gradient effects, it would be a good sign that properly sized textures can at least somewhat constrain spot growth. Simulations and experiments would need to be performed to determine optimum texture size and shape.

Finally, the tracking of fluid particles leads to the conclusion that the spot spreads by destabilizing the surrounding laminar boundary layer rather than by turbulent diffusion.

# References

J. Amini and G. Lespinard, "Experimental Study of an 'Insipient Spot' in a Transitional Boundary Layer," *Physics of Fluids*, Vol. 25, No. 10, Oct. 1982, pp. 1743-1750.

M. Bruse, D. W. Bechert, J. G. Th. van der Hoeven, W. Hage, and G. Hoppe, "Experiments with Conventional and with Novel Adjustable Drag-Reducing Surfaces," Near-wall Turbulent Flows: Proceedings of the International Conference, Tempe, AZ, 1993, pp. 719-738.

G. E. Colmenero, "Turbulent Boundary Layer Control with Discrete Actuators Using Wall Information," Master's Thesis, Aerospace Engineering Department, The University of Texas at Austin, December 2004.

E. Coustols and A. M. Savill, "Turbulent Skin-Friction Drag Reduction by Active and Passive Means: Parts 1 and 2," Special Course on Skin-Friction Drag Reduction, pp. 8-1 to 8-55, March 2-6, 1992 in AGARD Report 768.

H. W. Emmons, "The Laminar-Turbulent Transition in a Boundary Layer - Part I," *J. Aeronautical. Sciences*, Vol. 18, No. 7, July 1951, pp. 490-498

M. Gad-El-Hak, R. F. Blackwelderf, J. J. Riley, "On the growth of turbulent regions in laminar boundary layers," *J. Fluid Mechanics*, Vol. 110, 1981, pp. 73-95.

D. B. Goldstein, R. Handler, and L. Sirovich, "Modeling a No-Slip Flow Boundary with an External Force Field," *J. Comp. Phys*., Vol. 105, 1993, pp. 354-366.

D. B. Goldstein, R. Handler, and L. Sirovich, "Direct Numerical Simulation of Turbulent Flow Over a Modeled Riblet Covered Surface," *J. Fluid Mechanics*, Vol. 302, No. 10, 1995, pp. 333-376.

D. B. Goldstein and T.-C. Tuan, "Secondary Flow Induced by Riblets," *J. Fluid Mechanics*, Vol. 363, 1998, pp. 115-151.

D. B. Goldstein, J. Cohen and V. Levinski, "DNS of Hairpin Vortex Formation in Poiseuille Flow Due to Two-hole Suction," Presented at 3rd AFOSR Int. Conf. on DNS and LES, Arlington, TX, Aug. 2001

R. A. Handler, E. W. Hendricks, and R. I. Leighton, "Low Reynolds Number Calculation of Turbulent Channel Flow: A General Discussion," NRL Memorandum Report 6410, 1989, pp. 1-103.

D. Henningson, P. Spalart, and J. Kim, "Numerical Simulations of Turbulent Spots in Plane Poiseuille and Boundary Layer Flow," *Physics of Fluids,* Vol. 30, No. 10, Oct. 1987, pp. 2914-2917.

Y. Katz, A. Seifert, and I. J. Wygnanski, "On turbulent spots in a laminar boundary layer subjected to a self-similar adverse pressure gradient," *J. Fluid Mechanics*, Vol. 296, 1995, pp. 185-209.

J. Kim, P. Moin, and R. Moser, "Turbulence Statistics in Fully Developed Channel Flow at Low Reynolds Number," *J. Fluid Mechanics*, Vol. 177, 1987, pp. 133-166.

G. B. Schubauer and P. S. Klebanoff, "Contributions to the Mechanics of Boundary-Layer Transition," NACA TN-3489, 1955.

G. B. Schubauer and P. S. Klebanoff, "Contributions to the Mechanics of Boundary-Layer Transition," NACA TR-1289, 1956

B. Singer and R. Joslin, "Metamorphosis of a Hairpin Vortex into a Young Turbulent Spot," *Physics of Fluids*, Vol. 6, No. 11, Nov. 1994, pp. 3724-3736.

B. Singer, "Characteristics of a Young Turbulent Spot," *Physics of Fluids*, Vol. 8, No. 2, Feb. 1996, pp. 509-521.

M. Van Dyke, *An Album of Fluid Motion*, The Parabolic Press, Stanford, CA, 1982.

F. M. White, *Viscous Fluid Flow*, 2nd ed., McGraw Hill, 1991, Chap. 4.

I. J. Wygnanski, M. Sokolov and D. Friedman, "On a Turbulent 'Spot' in a Laminar Boundary Layer," *J. Fluid Mechanics*, Vol. 78, 1976, pp. 785-819.

I. J. Wygnanski, M. Zilberman, and J. H. Haritonidis, "On the Spreading of a Turbulent Spot in the Absence of a Pressure Gradient," *J. Fluid Mechanics*, Vol. 123, 1982, pp. 69-90.

## Vita

James Strand was born in Dallas, Texas, on October 27$^{th}$, 1983, to Mark and Connie Strand.  He has one sister, Bethany, who is four and a half years younger.  He attended Grace Lutheran Elementary, Hardin Intermediate, Byrd Junior High, and Duncanville High School, from which he graduated as salutatorian.  James enrolled at The University of Texas at Austin in the fall of 2002, and graduated with highest honors in May of 2005 with a Bachelor of Science in aerospace engineering.  He received a National Defense Science and Engineering Graduate Fellowship from AFOSR, and has been studying fluid dynamics under Dr. David Goldstein since the summer of 2005.  He lives in Austin with his girlfriend, Cori Nolan.


Permanent address:    Department of Aerospace Engineering and Engineering Mechanics

The University of Texas at Austin

210 East 24$^{th}$ Street, W. R. Woolrich Laboratories

1 University Station, C0600

Austin, TX 78712-0235


This thesis was typed by the author.